Numerical Simulation of Cone-Jet Formation in Electrohydrodynamic Atomization

Liang Kuang Lim
MEBCS Program, Singapore-MIT Alliance, Singapore 117576, Singapore

Jinsong Hua
Institute of High Performance Computing, 1 Fusionopolis Way, #16-16 Connexis, Singapore 138632, Singapore

Chi-Hwa Wang
MEBCS Program, Singapore-MIT Alliance, Singapore 117576, Singapore; and Dept. of Chemical and Biomolecular Engineering, National University of Singapore, Singapore 117576, Singapore

Kenneth A. Smith
MEBCS Program, Singapore-MIT Alliance, Singapore 117576, Singapore; and Dept. of Chemical Engineering, Massachusetts Institute of Technology, Cambridge, MA 02139

DOI 10.1002/aic.12254
Published online April 22, 2010 in Wiley Online Library (wileyonlinelibrary.com).

Electrohydrodynamic atomization (EHDA) process has received more research attention in recent years due to its potential to generate monodisperse droplets of low electric conductivity. It is reported that the EHDA process can be fine-tuned by adjusting the electrical field strength by an additional ring electrode near the nozzle tip to control both the spray mode and the droplet size. In the present study, a computational fluid dynamic (CFD)-based front tracking/finite volume method has been used to investigate numerically the effect of the secondary electric field source and the ring electrode on the EHDA process. The full Navier–Stokes equations are solved for both the liquid phase and the ambient air near the nozzle tip, and the liquid–air interface is monitored using a front tracking approach. At the interface, both the surface tension and the electrical stress due to surface charging and the applied electric field are taken into account. Because of the large dimension difference between the Taylor cone and the liquid jet, the simulations involve two drastically different length scales for describing the dynamic of the entire process. To accurately include the effect of the ring electrode, the electrical field distribution is first calculated over a domain large enough to enclose all key components of the EHDA process. Subsequently, the calculated electrical field in the large domain is integrated with the detailed CFD analysis on a small domain near the region of the nozzle tip. The formations of the Taylor cone, liquid jet, and droplets are successfully simulated and compared with experimental results with reasonable agreement. The numerical simulation method proposed in this article can be used as a platform for the investigation, analysis, and optimization of electrohydrodynamic atomization process. © 2010 American Institute of Chemical Engineers *AIChE J,* 57: 57–78, 2011

Correspondence concerning this article should be addressed to C.-H. Wang at chewch@nus.edu.sg
Current address of Jinsong Hua: Dept. of Process and Fluid Flow Technology, Institute for Energy Technology, P.O. Box 40, Kjeller NO-2027, Norway

Keywords: electrohydrodynamic, computational fluid dynamics, cone-jet formation, droplet formation, electrical field

Introduction

Electrohydrodynamic atomization (EHDA) has been observed and documented over a century.[1–4] Recently, there has been a renewed interest in exploring its ability to produce monodisperse liquid droplets for the fabrication of monodisperse polymeric particles[5–7] (Figure 1). Typically, an electrohydrodynamic spraying system consists of a nozzle, a high voltage direct current (DC) power supply attached to the nozzle to raise its electrical potential to the kilovolt range relative to earth, and an earthed ground electrode placed directly beneath the nozzle to act as the counter electrode in the system. When a liquid solution is pumped through the nozzle, and the solution emerges from the nozzle, electrical stresses will exert on the liquid–air interface to accelerate the liquid, and a cone-like structure, termed as "Taylor cone," is formed at the nozzle tip. Subsequently, a jet emerges from the tip of the Taylor cone at high speed,[8,9] and breaks into droplets due to the interfacial instability. As the jet and its physical characteristics are originated from the Taylor cone, an understanding of the formation of the Taylor cone is essential to the comprehension of governing physics for the EHDA processes.

In the process of electrohydrodynamic atomization, the electrical stresses play a key role in the Taylor cone-jet formation and jet breakup. Three different charge transport models, namely perfect conductor[1] model, perfect dielectric[10,11] model, and leaky dielectric[12–14] model, have been introduced to account for the electric charge transport in the electrohydrodynamic atomization process and to evaluate the electrical stress due to the electric charge-field interaction. In the case of a perfect conductor, it is assumed that the charge relaxation time is shorter than the system time constant and that charges exist only on the surface of the jet. No electric field exists inside the jet and the direction of the electric field on the surface of the jet is normal to the surface. A good representation of this kind of EHDA process is the spray of liquid metal. For the case of perfect dielectric, there is no conduction of electric charge. In this case, electric fields exist both inside and outside the liquid phase, and the electrical stress is manifested as a surface electrical polarization stress due to the interaction of the liquid and the electric field. As there is no electric charge in the system, the electric charge-field interaction stress is also absent in the system. An example of such perfect dielectric fluid might be heptane that is completely free from contaminants. Unfortunately, neither the aforementioned limiting models can adequately describe the typical EHDA spray of most chemical solvents. To overcome such limitations, the leaky dielectric model, which exhibits both the surface electric charge feature of the perfect conductor model and the electrical polarization stress of the perfect dielectric model, has been developed[15] and applied extensively for the analysis of EHDA process in recent years.[13–15]

In addition to the development of different charge transport models, previous theoretical studies have artificially divided the Taylor cone and the jet emitted from the tip of the cone, so that the analysis could be done for either Taylor cone or jet instability[16] separately. For the case of the Taylor cone, Shtern and Barrero[17] have analyzed the fluid flow in the Taylor cone based on the conical similarity class of exact solutions of the Navier–Stokes equations, and identified a few interesting features, including the circulatory motion of fluid inside the Taylor cone. The jet stability in electric field had been previously studied theoretically under different assumptions, including perfect dielectric,[11,12] perfect conductor,[1] and leaky dielectric[13–15] cases. Taking into account the effect of the electric charge-field interaction stress and the polarization stress on the stability of the jet, the presence of electric charges destabilizes the jet while the presence of the polarization stress stabilizes the jet. Such models with the separation of the Taylor cone and jet works well for the case where the liquid conductivity is high in the EHDA spray,

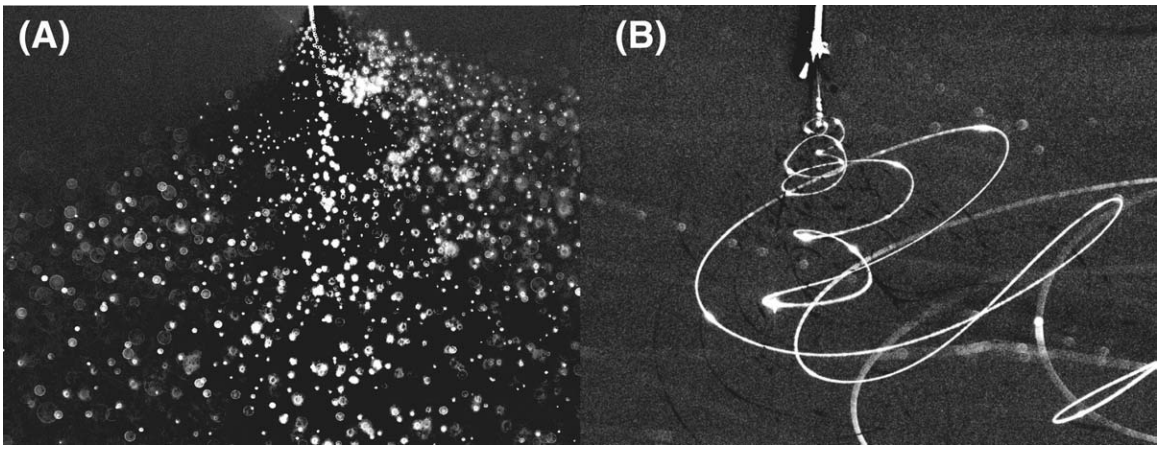

Figure 1. A: Electrohydrodynamic atomization for the fabrication of microdroplets and nanodroplets. B: Electrospinning for the fabrication of microfibers and nanofibers.

since there is a large size difference between the Taylor cone and the diameter of the jet[17] (with a ratio larger than the order of 10^3). However, a comprehensive understanding of Taylor cone-jet based on theoretical analysis in the case of low conductivity fluid, where the size difference between the Taylor cone and jet is about two orders of magnitude, has not been achieved due to the complicated nature of the coupling between the Taylor cone and jet.

Recently, CFD-based numerical simulations have been used to investigate the formation mechanism of the Taylor cone and jet. Hothman[18] and Hartman[19] simulated the formation of a Taylor cone and jet by solving a one-dimensional (1D) conservation of momentum equation to track the evolution of the liquid–gas interface. Unfortunately, such 1D simulations are unable to capture any radial motion of the fluid inside the Taylor cone. Hartman has further assumed a 1D electric field in the longitudinal direction, whereas the 2D nature of the electrical field near the nozzle was taken into account. In their works, the shape of the Taylor cone was calculated by solving a force balance on the surface of the Taylor cone. The liquid flow inside the Taylor cone was assumed to be unidirectional. Charge transport was taken into account by considering instantaneous electrical conduction in the bulk flow inside the Taylor cone and also convection of the electric charges on the surface of the Taylor cone. This results in a gradual accumulation of electric charges on the interface due to the conduction from the bulk of the liquid. As a result, the charge density at the interface is needed for the evaluation of the electrical stress on the liquid–air interface. Because of the instantaneous nature of the electrical conduction in the liquid bulk, there is no charge present in the liquid bulk and no electrical stress is observed there.

Yan et al.[20] proposed a 2D axisymmetric model to simulate the deformation of the electrically driven liquid meniscus in the cone-jet mode. The axisymmetric equations of continuity, momentum, and electric potentials are solved numerically. This model is able to calculate the shape of the liquid cone and the resulting jet, the velocity field inside the liquid cone-jet, the electric field inside and outside the cone-jet, and surface charge at the liquid surface. Even though this model could produce very comprehensive simulation results, the simulation algorithm is still quite complex in dealing the free surface. Their modeling algorithm was not extended further to account for the drop formation from the liquid jet. Lastow[21] performed a two-dimensional simulation using the commercial software package CFX 4.4 without taking into account the electrical current in the system. The Navier–Stokes equation with additional electrical stress term was solved for the momentum balance, and Poisson's equation was solved for the field distribution of electric potential. Using this method, the circulatory feature of the flow inside the Taylor cone was reproduced. One limitation in all aforementioned simulations is that they are unable to capture the formation of droplets.

The recent development of front tracking method for multiphase flow[22,23] simulation has provided a novel and robust numerical approach to treat the moving interface between two fluids with large density difference. Such method has been applied successfully in various interfacial flow problems.[24] In this study, to simulate the electrohydrodynamic atomization process, the Navier–Stokes equation is modified to take into account the electrical stresses on the interface. The front tracking/finite volume method proposed by Hua and Lou[24] is further extended to take into account the electric charge on the liquid–gas interface and the interface movement in the coupled electric and fluidic fields. In this method, a stationary fixed grid is used throughout the whole computational domain for the fluid flow and electric fields, and a set of adaptive elements is used to mark the position of the moving interface. Only one set of Navier–Stokes equations is solved in the whole computational domain by treating the different phases as one single fluid with variable material properties. The distributions of physical properties such as density, viscosity, and electrical permittivity are calculated according to the position of the interface and the property difference of two fluid phases. Interfacial source terms such as surface tension and electric charge-distribution are computed on the front and then transferred to the fixed background grid through the use of a dirac-delta function for interpolation. The position of the interface is advected explicitly with the velocity interpolated from the flow field on the background gird.

The electric field is a key parameter in determining the electrical stresses exerted on the liquid–gas interface. Hence, it is important to estimate the electric field accurately, especially at the region near the nozzle tip where the Taylor cone and the liquid jet are formed. The presence of the Taylor cone and jet has little effect on the electric potential field at the far field (about 10 nozzle diameter away from the Taylor cone and jet). Hence, the electrical potential field is first calculated in the much larger domain (enclosing all key parts of the EHDA process), which includes the electrodes and the far field potentials, to get the nonuniform electrical potential distribution at the region near the nozzle tip. Then, with proper boundary conditions for fluid flow and also the electrical potential boundary conditions derived from the electrical potential field calculation in the large domain, the detailed fluid flow as well as the electric field is calculated over a small domain for the region near the nozzle tip. Transient simulations are also performed on the small domain to investigate the formation of the Taylor cone and jet in electrohydrodynamic atomization, taking into account the coupling among the two-phase fluid flow dynamics, moving interface and electric field. The simulation results are then compared with experimental observation for evaluation of the accuracy.

In brief, the cone-jet formation of the EHDA process was simulated in the current work using the front tracking/finite volume method whereby the electrical stresses is coupled into the Navier–Stokes equation. These simulations aim at systematic investigation on the adjustment of the ring electrode potential for achieving fine control of the droplet formation in EHDA process. The rest of the article is arranged as follows. First, the experimental methods through which the experimental data were obtained are presented. The numerical models are set up according to the parameters used in the experiments so that the results from simulations and experiments could be compared. Following that, the numerical modeling strategy to capture the details about cone-jet formation is introduced. The governing equations for liquid–gas flow and electric potential field calculation, the treatment

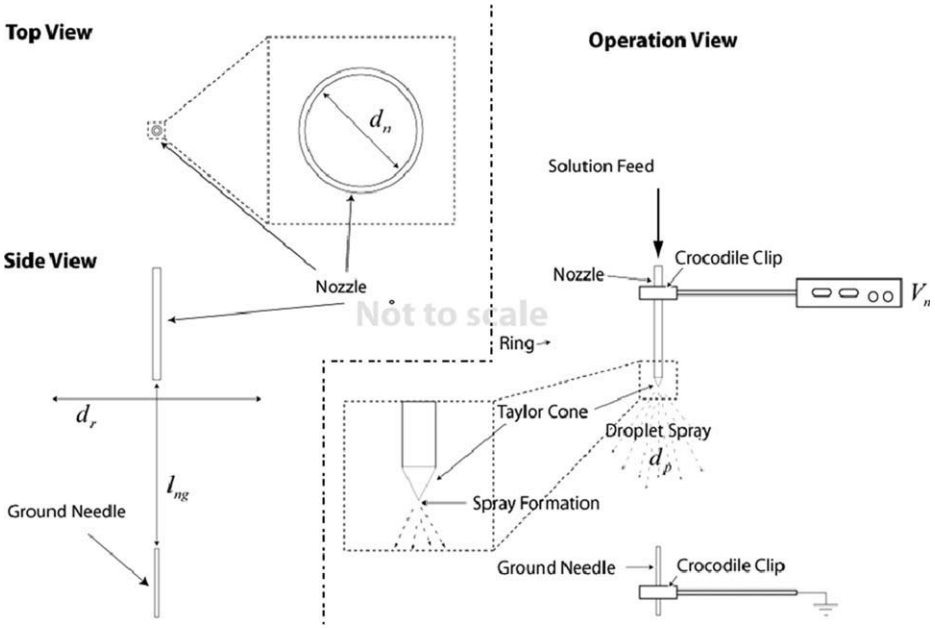

Figure 2. Schematics for the experimental setup.

of moving interface, surface tension and surface charge, and the numerical solving approach such as non-dimensionalization and numerical methods are depicted in detail in the following sections. The numerical simulations results are then presented and compared with the experiments, and further discussion is given as well. Finally, the conclusions drawn from this study are summarized.

Physical Problem and Modeling Strategy

Experimental setup for electrohydrodynamic atomization

The experimental setup for the electrohydrodynamics atomization is shown in Figure 2. In the present system, two separate electrodes were included to act as the electric potential field sources. The nozzle was made from a 29 gauge spinal tap needle (Becton Dickinson) with the sharp tip cut and filed to form a flat tip. It has an outer diameter of 340 μ and an inner diameter of 220 μ. It was connected to a Glassman high voltage DC power supply (V_n). The second electrode was in the form of a ring, which is placed slightly above the outlet of the nozzle, and coaxially with the nozzle. The ring electrode was made from a copper tube with outside diameter of 2 mm and formed into a ring with a diameter of 40 mm (d_r). The center of the ring electrode was placed 10 mm (l_{nr}) above the tip of the nozzle, and was connected to another separate Glassman high voltage DC power supply (V_r). This arrangement enabled the nozzle electrical potentials on the nozzle and ring electrodes to be varied independently. An additional 29 gauge spinal tap needle was located 100 mm (l_{ng}) below the tip of the nozzle. It was connected to ground and was used to act as the counter electrode to the nozzle and the ring electrodes. Thus, the difference of electrical potential settings on the nozzle and the ring electrodes (V_n, the nozzle electrode to the grounded needle or V_r, the ring electrode to the grounded needle) modulated the electric field near the nozzle tip. Ijsebaert[25] has previously made use of the ring electrode in his study of the production of aerosols, but the ring potential was set to a constant and was thought only to have the effect of focusing the spray. In the current study, the ring acted as a method to control the electric field strength near the tip of the nozzle, where the Taylor cone and jet were formed and tuned by the electric field.

Photographs were taken with a digital SLR camera (D2H, Nikon, Japan) with a macro lens (105 mm Micro Nikkor, Nikon, Japan) for high magnification. Pictures were taken using a cold cathode fiber optic illuminator (Model 41500-55, Cole Parmer Instrument Company) to provide back lighting, with an aperture size of F-25 and a shuttle speed of 1/2000 s.

Droplet size was measured with a laser-based phase Doppler particle analyzer (TSI, Minneapolis, MN). The phase Doppler method is based upon the principles of light scattering interferometry. Measurements are made in a small optical probe volume defined by the intersection of two laser beams. As a particle passes through the probe volume, it scatters light from the beams into a multi-detector receiving probe, strategically located at an off-axis collection angle. The phase shift between the Doppler burst signals from different detectors is proportional to the size of the spherical particles.

Modeling strategy

Because of the small size of the cone-jet and the droplet formed, it is quite difficult to measure the detailed flow dynamics and electrical field inside the liquid phase, as well as the electric charges on the liquid–gas interface. To investigate the electrohydrodynamic atomization process, some simplifications and assumptions have to be made in the analysis due to the physical complexity of the problem, for example, by splitting the Taylor cone and jet into two different phenomena as mentioned before in the previous sections.

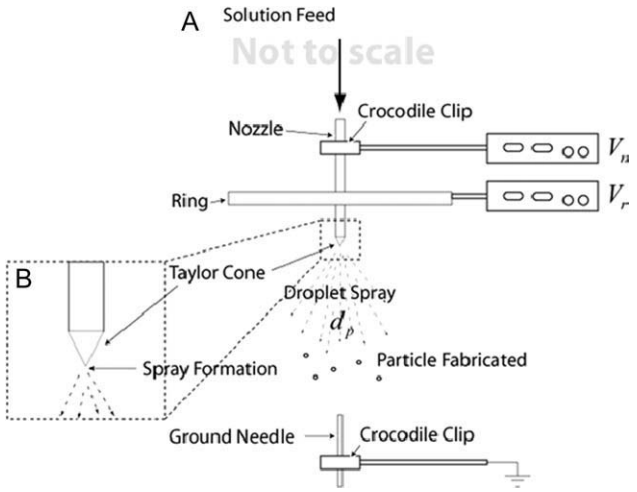

Figure 3. Simulation domain.

Domain A includes the nozzle, the ring, and the ground needle and is used for electrical field calculation. Domain B is at the tip of the nozzle and is used for CFD simulation. The nozzle and ring are connected to the high voltage power supply V_n and V_r, respectively.

Fortunately, the first-principle-based CFD simulations provide us with an alternative approach to investigate the complex coupling phenomena in EHDA.

For the accurate estimation of electric field, a large domain encompassing all the different entities (Figure 3, Domain A) is required. However, the larger domain required for the electric field calculation is prohibitively too large for the CFD simulation, since the CFD simulation is more computationally expensive than the electric field calculation. In addition, the interested region for the CFD simulation is much smaller (confined to the region near the nozzle outlet) compared to that for the electric field calculation (encompassing all the electrodes of nozzle, ring, and ground). This is due to the small inner radius of the nozzle (R_0) as compared to the distances among the nozzle, the ring electrode, and the ground needle (e.g., $l_{ng}/R_0 \approx 950$). For instance, the ring electrode is located at the position about 90 R_0 away from the nozzle and the ground is located at a position about 900 R_0 away. Therefore, it is not a good approach to perform the CFD simulation on the same simulation domain as the one required for the electric field calculation. Fortunately, the liquid flow changes the electric field only locally, and the electric field strength at certain distance from nozzle outlet will be almost unaffected by the presence of liquid jet. This suggests that only the electric field distribution needs to be solved for the large domain (Figure 3, Domain A), while the governing equations for both fluid flow and electrical field are solved over a smaller domain near the nozzle tip (Figure 3, Domain B) to capture the details of the fluid flow and its interaction with the electric field.

To study the electric effect of the ring electrode and ground needle while keeping the simulation domain reasonably small, the electrical potential field in Domain A would be first calculated using the Laplace's equation without taking into account the liquid flow in the system. Here, the nozzle electrical potential and the ring electric potential are both taken into account, and the simulation geometry matches the actual production facilities (Figure 3, Domain A). Once the electric potential field is calculated in Domain A, the electric potential value on the boundary of the CFD simulation domain is extracted, and applied onto the CFD simulation as the electric potential boundary conditions (Figure 3, Domain B; Figure 4). During the CFD simulation, the Poisson's equation for the electric potential is solved again to obtain the detailed electric field near the nozzle tip for the electrical stress calculation. When the stable Taylor cone and jet are reached, the Taylor cone angle and the jet diameter will remain constant. The electric potential field in Domain A is then recalculated with the liquid phase, which is determined with the CFD simulation in Domain B. The two different sets of results of electric potential field calculation in Domain A, one without the liquid phase and one with the liquid phase, are compared and checked for convergence. The whole process of simulation ends when the convergence of the electric potential field calculation in Domain A is achieved. The size of Domain B must be properly selected such that convergence of the electric potential field calculation in Domain A can be achieved and justified.

In the present study, a CFD simulation domain (shown in Figure 4) was chosen in a cylindrical coordinate system with the size of 24 R_0 in the axial direction and 3 R_0 in the radial direction. Here, R_0 is the inner radius of the nozzle. The simulation was performed on a fixed grid mesh of 120 $\times$ 960 and the nozzle radius is meshed with 40 grids per unit dimensionless length scale ($=R_0$). The mesh should be fine enough to reasonably capture the fluid flow behavior nearby the nozzle tip according to the mesh sensitivity analysis that

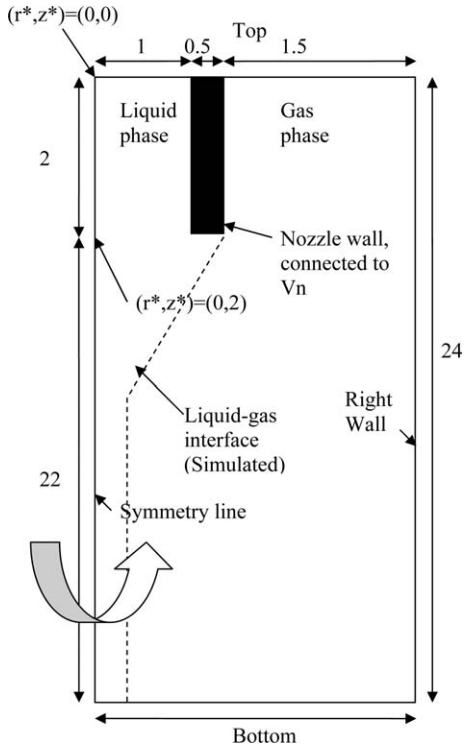

Figure 4. CFD simulation domain (Figure 3, Domain B).

Dimension length is normalized by the nozzle radius. (r^*, z^*) = (r/R_0, z/R_0), where r and z refer to the dimensional, radial, and axial direction coordinates, respectively.

has been performed in the previous work of Hua and Lou[23] for the front tracking/finite volume method. The left wall was the symmetry axis of cylindrical coordinate system. Zero gradient of electrical potential was imposed along the normal direction on the top boundary. This is because the electric field is in the direction perpendicular to the outer nozzle wall. On the right and bottom wall, in contrast, the boundary conditions were extracted directly from the electrical field calculation on Domain A. Note that the gravity in this domain is acting from the top to bottom. The selected size for Domain B has been checked for convergence, as presented in the previous paragraph, to ensure that the selection of domain size has no observable variation on the final results.

Mathematical Formulation

Governing equations for fluid flow

The flow field simulation is formulated by solving the governing equations of mass conservation and the Navier–Stokes equations. For the EHDA system, it consists of two phases, the liquid phase and the gas phase (ambient air). In addition, the multiphase flow is coupled with the applied electric potential field and electric charging on the interface. Assuming the system to be isothermal, both liquid and gas phases can be considered incompressible. Hence, the mass conservation of the whole domain, which consists of both the gas phase and the liquid phase, can be expressed as,

$$\nabla \cdot \vec{u} = 0, \tag{1}$$

where $\vec{u}$ is the velocity of the fluid.

To take into account the surface tension on liquid–gas interface (F_{ST}), the electrical stresses (F_{ES}) and gravitational force, the Navier–Stokes equation would need to include the additional terms for these forces and can be expressed as,

$$\frac{\partial \rho \vec{u}}{\partial t} + \nabla \cdot \rho \vec{u}\vec{u} = -\nabla p + \nabla \cdot \left[\mu\left(\nabla \vec{u} + \nabla \vec{u}^{T}\right)\right] + (\rho - \rho_g)\vec{g} + \vec{F}_{ST} + \vec{F}_{ES}, \tag{2}$$

where ρ is the density of the fluid, p is the pressure, μ is the viscosity of the fluid, $\vec{g}$ is the gravitational acceleration. Subscript g refers to the gas phase.

The surface tension force on the liquid–gas interface can be calculated as follows,

$$\vec{F}_{ST} = \int_{\Gamma} \gamma \kappa \vec{n} \delta\left(\vec{x} - \vec{x}_f\right) ds_f, \tag{3}$$

where γ is the surface tension coefficient, κ is the curvature of the interface, Subscript f refers to the front or interface. $\delta(\vec{x} - \vec{x}_f)$ is a dirac-delta function, which is used to impose the surface tension force acting on the perimeter of the control volume where the interface is located.

The electrical volume stress[26] can be calculated by taking the divergence of the Maxwell stress tensor (σ^M) while assuming that the fluid is incompressible,

$$\vec{F}_{ES} = \nabla \cdot \sigma^M = -\frac{1}{2}\vec{E} \cdot \vec{E}\nabla \varepsilon + q^v \vec{E}, \tag{4}$$

where $\vec{E}$ is electric field, ε is the permittivity of fluid, and q^v is the volume charge density near the interface. The first term on the right of Eq. 4 is due to the polarization stress, and it acts in the normal direction of the interface as a result of the term $\bigtriangledown \varepsilon$. The second term, due to the interaction of the electric charges with the electric field, acts in the direction of the electrical field. As it was assumed that the electric charges are located on the interface, both the polarization electrical stress and the charge-field interaction electrical stress would thus be exerted on the interface.

Governing equations for electric field

Poisson's equation for electrical potential calculation is given as:

$$\nabla \cdot (\varepsilon \nabla \phi) = q^v, \tag{5}$$

where ε is the electrical permittivity of the fluid, ϕ is the electric potential, and q^v is the volume charge density. The electric field $\vec{E}$ is related to the electric potential through the following equation,

$$\vec{E} = -\nabla \phi. \tag{6}$$

Note that at the interface, q^v is nonzero due to the distribution of electric charge, and ε is not constant since it will change as it crosses the moving interface from the liquid phase to gas phase. This will cause the electric field to change both in strength and direction as it crosses the liquid–gas interface.

Electric charge on interface

In the electrohydrodynamic atomization process, the liquid that emerges from the nozzle is charged electrically. The interaction between the electrical field, the electric charges, and also the liquid–gas interface (due to the varying electrical permittivity, causing a polarization stress) creates electrical stresses that will augment the normal flow dynamics, thus creating new flow forms.

To successfully simulate the electrohydrodynamic atomization process, it is important to obtain the proper estimation of the electric charge density on the interface as well as its distribution. The distribution of electric charge can be approximated by first considering two inter-related parameters, the electrical relaxation time of the system and the Debye length. The electrical relaxation time[27] is used to define the charge relaxation time in the electrohydrodynamic system. It is defined as the ratio of the electrical permittivity (ε) over the electrical conductivity (K),

$$\tau^E = \frac{\varepsilon}{K}. \tag{7}$$

The Debye length is related to the thickness of the electric charge boundary layer, where the electric charges will be located when it is distributed on the surface of an electrohydrodynamic system. The Debye length can be defined as

$$\lambda = \sqrt{D\frac{\varepsilon}{K}} = \sqrt{D\tau^E}. \tag{8}$$

Note that the molecular diffusivity of the charge species and the electrical permittivity of the system have a positive effect on increasing the Debye length, while increasing the electrical conductivity decreases the Debye length.

In the current study, dichloromethane is used as the liquid phase for the EHDA process. The relative permittivity is $\varepsilon = 7.73 \times 10^{-11}$, and the electric conductivity is about $K = 2.75 \times 10^{-8}$ S/m. Hence, the time scale of charge relaxation is estimated as $\tau^{\mathrm{E}} = 2.81 \times 10^{-3}$ (s). To have a better understanding about the scales of charge relaxation time, we also estimate the charge relaxation time in two publications by Ganan-Galvo et al.[28] and Lastow and Balachandran.[21] "Dioxane + 2% Formamide" was used in the work by Ganan-Galvo and colleagues.[28] The corresponding values for permittivity ($\varepsilon = 2.04 \times 10^{-11}$) and electric conductivity ($K = 2.4 \times 10^{-7}$ S/m) are used for estimating the time scale of charge relaxation, $\tau^{\mathrm{E}} = 8.48 \times 10^{-5}$ (s). In contrast, "Hptane + 0.1% Stadis" was used in the work by Lastow and Balachandran.[21] The corresponding values for permittivity ($\varepsilon = 1.68 \times 10^{-11}$) and electric conductivity ($K = 7.7 \times 10^{-7}$ S/m) are used for estimating the time scale of charge relaxation, $\tau^{\mathrm{E}} = 2.18 \times 10^{-5}$ (s). Hence, the charge relaxation time scale in the current study is much larger than the past work where leaky dielectric model is used. This also indicates that the fluid has a relatively low conductivity.

Leaky dielectric model was commonly used for the EHDA system when the charge relaxation time scale ($\tau^E = \frac{\varepsilon}{K}$) is much smaller than the time scale of viscous flow ($\tau^V = \rho L^2/\mu$).[21,28] In this study, the charge relaxation time scale is not small, and is about two orders higher than the previous studies. Hence, Leaky dielectric model is not suitable to estimate the charge density on the liquid–air interface. There is not any well developed theory to estimate the charge density on the interface when the liquid electric conductivity is relatively low. In this study, a constant surface charge density on the interface was assumed to simplify the charge transport problem on the interface.

In the numerical modeling, the charge on the interface is distributed to the control volume where the interface lies. Physically, this approximation would mean that the electric charge will thus be located in a thin layer on the surface of the electrohydrodynamic system. The interfacial (surface) charge density, q^{s}, was applied as an input to the simulation. The interfacial charge density is then distributed around the liquid–gas interface, so that a volume charge density, q^{v}, is obtained on the background grid to estimate the electrical stress for the momentum conservation calculation. The interfacial charge density is related to the volume charge density by,

$$q^{\mathrm{s}} = \int_{-l}^{l} q^{\mathrm{v}} dl \tag{9}$$

where the interface spans over a distance of $2l$. The surface charge density was assumed to be constant throughout. As there is no pre-simulation knowledge of the charge density on the liquid–gas interface, the charge density that gave the best fit of the profile of the Taylor cone and jet from the CFD simulation to the experimental data was chosen as the interfacial charge density through a trial-and-error approach.

Front tracking/finite volume method

Although the physical properties are considered to be constant in each phase, there is a change in the physical properties across the interface. To solve the Navier–Stokes equation in the whole domain using "one-fluid" formulation, the fluid physical properties should vary smoothly from the gas phase to the liquid phase. The front tracking/finite volume method has been previously deployed on modeling gas bubbles rising in liquid successfully. The novelty of the front tracking method, proposed by Tryggvason,[22] is that the interface (i.e., the moving front) is considered to have a finite thickness of the order of the mesh size, instead of zero thickness with sharp jump of fluid properties. In the region nearby the interface, the physical property distribution is reconstructed using an approximated delta function, and changes smoothly and continuously from the value on one side of the front to the value on the other side. The thickness of the interface thus depends on the grid size and is kept constant during the interface moving. Thus, the governing equations could be solved in all domains with variable fluid properties for the presence of both liquid and gas phases with an interface.

In the front tracking method, the interface is considered to have a finite thickness of the same order as the mesh size instead of zero thickness. In this interfacial transitional zone, the physical property changes smoothly and continuously from the value on one side of the interface to the value on the other side. The field distribution $b(\vec{x},t)$ of the physical properties of the fluid throughout the whole domain can be calculated through,

$$b(\vec{x},t) = b_{\mathrm{g}} + (b_{\mathrm{l}} - b_{\mathrm{g}}) \cdot \vec{I}(\vec{x},t) \tag{10}$$

where b_{l} is the properties in the liquid phase, b_{g} is the properties in the gas phase, and $\vec{I}(\vec{x},t)$ is an indicator function which has a value of one in the liquid phase and zero in the gas phase. The indicator function can be written in the form of an integral over the inner domain Ω enclosed by the interface,

$$\vec{I}(\vec{x},t) = \int_{\Omega} \delta\left(\vec{x} - \vec{x}_{\mathrm{f}}\right) dv_{\mathrm{f}} \tag{11}$$

where $\delta(\vec{x} - \vec{x}_{\mathrm{f}})$ is a delta function.

A distribution function $\vec{D}(\vec{x})$ is used to approximate the delta function and estimate the fraction of the physical properties distributed across the artificial thickness of the interface. In this study, the distribution function given by Peskin[29,30] is used.

$$D(\vec{x} - \vec{x}_{\mathrm{f}}) = \begin{cases} (4h)^{-2} \prod_{i=1}^{2} \left(1 + \cos\left(\frac{\pi}{2h}\left|x_i - x_{i,\mathrm{f}}\right|\right)\right), & \text{if } \left|\vec{x} - \vec{x}_{\mathrm{f}}\right| < 2h \\ 0, & \text{otherwise} \end{cases}, \tag{12}$$

where h is the grid size, and i represents the directions of the coordinate system. With the distribution function, the force on the interface can be distributed into the volume of the background mesh using the following expression,

$$\vec{F}_{\mathrm{ST,f}} = \gamma \kappa_{\mathrm{f}} \vec{n}_{\mathrm{f}}, \tag{12a}$$

$$\vec{F}_{\mathrm{ST}} = \int_{\mathrm{f}} \gamma \kappa_{\mathrm{f}} \vec{n}_{\mathrm{f}} D(\vec{x} - \vec{x}_{\mathrm{f}}) ds_{\mathrm{f}} = \sum \vec{F}_{\mathrm{ST,f}} D(\vec{x} - \vec{x}_{\mathrm{f}}) \Delta s_{\mathrm{f}}. \tag{12b}$$

In a similar manner, the electric charges on the drop surface can be distributed to the vicinity volume to obtain volume charge density as

$$q^{\mathrm{v}} = \sum_{\mathrm{f}} q^{\mathrm{s}} D(\vec{x} - \vec{x}_{\mathrm{f}}) \Delta s_{\mathrm{f}}. \tag{12c}$$

Taking the gradient of the indicator function $I(x,t)$, a gradient function $\vec{G}(\vec{x},t)$, showing the changes cross the interface, is given as follows in an integral form,

$$\vec{G}(\vec{x},t) = \nabla I(x,t) = \sum\nolimits_{\mathrm{f}} D(\vec{x} - \vec{x}_{\mathrm{f}}, t) \vec{n}_{\mathrm{f}} \Delta s_{\mathrm{f}} \tag{13}$$

where $\vec{n}_{\mathrm{f}}$ is the unit normal at the interface at an interfacial element with an area of Δs_{f} whose centroid is $\vec{x}_{\mathrm{f}}$. Hence, the indicator function can be reconstructed using the following equation,

$$\nabla \cdot \nabla I(x,t) = \nabla \cdot \vec{G}(x,t) \tag{13a}$$

With the calculated distribution of fluid property and also the force source in governing equations, the velocity field is obtained on the fixed background mesh. The moving velocity of the interface could be interpolated from the velocity field at the fixed grid so that the interface is ensured to move at the same velocity as the surrounding fluids. The distribution function given by Peskin is used to interpolate the velocity of the interface from the background field using,

$$\vec{u}_{\mathrm{f}} = \sum D(\vec{x}_{\mathrm{f}} - \vec{x}) \vec{u} \tag{14}$$

Then, the interface is advected in a Lagrangian fashion,

$$\vec{x}_{\mathrm{f}}^{\,n+1} - \vec{x}_{\mathrm{f}}^{\,n} = \Delta t \, \vec{u}_{\mathrm{f}} \tag{15}$$

After the interface is advected, the mesh size and quality on the interface (front) may be deteriorated due to the deformation of the front. Hence, front mesh adaptation has to be performed to improve the front mesh quality.

Numerical Methods

Non-dimensionalized system

The selection of a suitable non-dimensionlization for the above problem has proved to be an intricate consideration due to the drastic length scale difference between the electrical system (nozzle, ring, and ground needle) and the fluid flow system (the liquid ejected from the tip of nozzle). After careful consideration, it was determined that two different length scales should be used, one for the electrical system and one for the fluid flow system, to track this multi-scale system by suitable non-dimensionalization schemes. As shown in the previous section, the choice of using two different length scales stems from the large difference in dimensions between the electrical system and the flow system, and this further rationalizes the division of the simulation work into two parts to facilitate computational work.

For the electrical potential system, a suitable length scale should be the distance between the nozzle and the ground needle, which is in the centimeter range in the present model configuration. This is due to the fact that the electrical field is distributed throughout the whole region where the nozzle, the ring, and the ground needle are present, and the changes in the strength of the electrical field is largely dependant on the position of each particular point in space relative to the nozzle and the ground needle. This observation justifies the first length scale λ_1 as,

$$\lambda_1 = l_{\mathrm{n-g}} \tag{16}$$

where $l_{\mathrm{n-g}}$ is the distance between the nozzle and ground electrodes. The typical value of $l_{\mathrm{n-g}}$ is fixed to 10 cm in the current study case. For the liquid flow system, a suitable length scale can be the inner diameter of the nozzle. As the liquid jet is emerging from the nozzle, the second length scale can be chosen as the inner radius of the nozzle, R_0,

$$\lambda_2 = R_0 \tag{17}$$

Henceforth, the ratio of these two time scales is given by

$$\frac{\lambda_2}{\lambda_1} = 0.0017 \tag{18}$$

The ratio clearly shows that the difference in length scale is around 3 orders of magnitude. The suitable length scale for describing the electrical charge system should be the same as the liquid flow system since the electrical charge resides predominately in the liquid flow. The electrical potential can be non-dimensionalized with reference to the potential difference between the nozzle and the ground needle, $\phi^* = \frac{\phi}{\phi_{\mathrm{n}}}$, where ϕ_{n} is the dimensional potential difference between the nozzle and the ground needle. The permittivity (ε) is non-dimensionalized with reference to the permittivity of air (ε_{g}), which is the outer fluid, as $\varepsilon^* = \frac{\varepsilon}{\varepsilon_{\mathrm{g}}}$.

Using the two length scales discussed above, and applying the suitable length scale for the different terms encountered in the modified Navier–Stokes equation, one can then determine the suitable dimensionless groups governing the physics of the system.

The characteristic electrical field strength scale $\widetilde{E}$ can then be defined using the first length scale as $\widetilde{E} = \frac{\phi_{\mathrm{n}}}{\lambda_1}$. And the dimensionless electric field strength can be defined as $\vec{E}^{\,*} = \frac{\vec{E}}{\widetilde{E}} = \frac{\vec{E} \cdot \lambda_1}{\phi_{\mathrm{n}}}$.

For the electrical system, the parameters are analyzed through the Poisson's Equation (Eq. 5), $\nabla \cdot (\varepsilon \nabla \phi) = q^{\mathrm{v}}$. Conversely, the characteristic volume charge density $\tilde{q}^{\mathrm{v}}$ can be determined through the Poisson's equation (Eq. 5) as $\tilde{q}^{\mathrm{v}} = \frac{\varepsilon_{\mathrm{g}} \phi_{\mathrm{n}}}{\lambda_2^2}$. In the above expression, λ_2 was used as the length scale since the electrical charge is only located in the liquid flow system. The non-dimensional volume charge density can be defined as $q^* = \frac{q^{\mathrm{v}}}{\tilde{q}^{\mathrm{v}}}$. The surface charge density can be

obtained by the integral of the volume charge density q^v across the interface as $q^s = \int q^v dl$. Hence, the characteristic surface charge density can be defined as $\tilde{q}^s = \frac{\varepsilon_g \phi_n}{\lambda_2}$. The non-dimensional surface charge density is given as $q^{*s} = \frac{q^s}{\tilde{q}^s} = \frac{q^s \cdot \lambda_2}{\varepsilon_g \phi_n}$.

Conversely, for the fluid flow system, the parameters are determined through the balance of the viscous term against the electric stress term along the tangential direction (Eq. 4) due to charge at the interface.

$$\nabla \cdot (\mu(\nabla \bar{u} + \nabla \vec{u}^T)) \cdot \vec{T} \sim q^v \vec{E} \cdot \vec{T}. \tag{19}$$

where $\vec{T}$ is the unit vector in the tangential direction and the surface charge density can be assumed as $q^s \sim q^v \cdot \lambda_2$. The scale analysis of Eq. 19 indicates $\frac{\tilde{u}\mu_l}{\lambda_2^2} \sim \frac{q^s \lambda_2 \phi_n}{\lambda_1}$. Hence, the characteristic velocity ($\tilde{u}$) and time scales ($\tilde{t}$) can be defined as,

$$\tilde{u} = \frac{\lambda_2}{\lambda_1} \frac{q^s \phi_n}{\mu_l}, \quad \tilde{t} = \frac{\lambda_2}{\tilde{u}} = \frac{\lambda_1 \mu_l}{q^s \phi_n} \tag{20}$$

Hence, the fluid velocity can be non-dimensionalized as $\vec{u}^* = \vec{u}/\tilde{u}$, the time as $t^* = t/\tilde{t}$.

Some additional dimensionless parameters required by the final dimensionless form of the governing equation are given by,

$$\rho^* = \frac{\rho}{\rho_l}, \quad \mu^* = \frac{\mu}{\mu_l}, \quad \vec{g}^* = \frac{\vec{g}}{|\vec{g}|}. \tag{21}$$

After non-dimensionalization, the electrical potential field can be calculated through the following equation,

$$\nabla \cdot (\varepsilon^* \nabla \phi^*) = -q^{*v} \tag{22}$$

The modified momentum equation can be re-expressed in the following dimensionless form:

$$\frac{\partial \rho^* \vec{u}^*}{\partial t^*} + \nabla \cdot \rho^* \vec{u}^* \vec{u}^* = -\nabla p^* + \frac{1}{\mathrm{Re_E}} \nabla \cdot \left[\mu^* \left(\nabla \vec{u}^* + \nabla \vec{u}^{*T} \right) \right] + \frac{1}{\mathrm{Gr_E}} (\rho^* - \rho_g/\rho_l) \vec{g}^* + \frac{1}{\mathrm{Bo_E}} \int_f \kappa_f^* \vec{n}_f \delta(\vec{x} - \vec{x}_f) ds_f - \frac{1}{El_P} \frac{1}{2} \vec{E}^* \cdot \vec{E}^* \nabla \varepsilon^* + \frac{1}{El_C} q^{*v} \vec{E}^* \tag{23}$$

The non-dimensionalized momentum equation has provided the following five different terms ($\mathrm{Re_E}$, $\mathrm{Gr_E}$, $\mathrm{Bo_E}$, $\mathrm{El_P}$, $\mathrm{El_C}$) to characterize the relative importance of the different stresses in the physical system.

The first dimensionless group is the electrical Reynolds number for the relative importance of the viscous stress,

$$\mathrm{Re_E} = \frac{\rho_l \tilde{u} \lambda_2}{\mu_l} = \frac{\lambda_2^2}{\lambda_1} \frac{\rho_l q^s \phi_n}{\mu_l^2}, \tag{24}$$

This is followed by the electrical gravitational number ($\mathrm{Gr_E}$) for the relative importance of gravity,

$$\mathrm{Gr_E} = \frac{\tilde{u}^2}{\left|\vec{g}\right| \cdot \lambda_2} = \frac{\lambda_2}{\lambda_1^2} \frac{(q^s)^2 \phi_n^2}{\mu_l^2 \left|\vec{g}\right|}, \tag{25}$$

Third, the electrical Bond number ($\mathrm{Bo_E}$) is given for the relative importance of the surface tension stress,

$$\mathrm{Bo_E} = \frac{\rho_l \tilde{u}^2 \lambda_2}{\gamma} = \frac{\lambda_2^3}{\lambda_1^2} \frac{\rho_l (q^s)^2 \phi_n^2}{\gamma \cdot \mu_l^2}, \tag{26}$$

Fourth, the electrical polarization number ($\mathrm{El_p}$) is introduced for describing the relative importance of the polarization stress in the system which is created due to the change in electrical permitivity across the interface,

$$\mathrm{El_P} = \frac{\rho_l \tilde{u}^2}{\tilde{E}^2 \varepsilon_g} = \frac{\lambda_2^2 \rho_l (q^s)^2}{\varepsilon_g \mu_l^2}. \tag{27}$$

Finally, the electrical coulombic number ($\mathrm{El_C}$) is given for the relative importance of the coulombic stress, due to the interaction of the surface charge with the electrical field.

$$\mathrm{El_c} = \frac{\rho_l \tilde{u}^2}{\lambda_2 \tilde{q}^v \tilde{E}} = \frac{\lambda_2^3}{\lambda_1} \frac{\rho_l (q^s)^2}{\varepsilon_g \mu_l^2}. \tag{28}$$

In the present work, the momentum equation is discretized using the finite volume method on a fixed, staggered, uniform Cartesian grid. As the front is advected explicitly, the physical properties and surface tension are updated subsequently. Then, the coupling fluid velocity and pressure are updated by solving the momentum equations and the continuity equation using SIMPLE scheme.[31] The simulation process is thus robust even for large density ratio because of the semi-implicit solving approach.

The liquid phase has the physical properties of dichloromethane, which was used as the reference liquid: density $\rho_l = 1360$ kg/m^3, viscosity $\mu_l = 4.3 \times 10^{-4}$ Pa s, relative electrical permittivity $\varepsilon_l = 8.73$, and surface tension $\gamma = 0.0254$ N/m. The gas phase has physical properties of the normal atmospheric ambient air (density $\rho_g = 1.25$ kg/m^3, viscosity $\mu_g = 1.8 \times 10^{-6}$ Pa s, relative electrical permittivity $\varepsilon_g = 1$). The nozzle has an outer radius of 170 μ and an inner diameter of 110 μ. The gravitational acceleration is 9.81 m/s^2 and the electrical permittivity of vacuum is 8.85×10^{-12} F/m. The rest of the physical properties were kept constant throughout unless stated otherwise. For a nozzle voltage of 8 kV relative to ground, the value of the electrical field strength calculated by assuming constant field strength between the nozzle and the ground needle is about 80,000 V/m. In contrast, the electrical field strength in the Taylor cone and jet (the tip of the nozzle is more like a point source, so a nonuniform electrical field in the z direction does exist) is typically of the order of 1,000,000 V/m, with the field decaying in strength as we move further away from the nozzle.

Numerical procedure

As explained in the previous section on modeling strategy, we adopt two levels of the numerical procedures in the

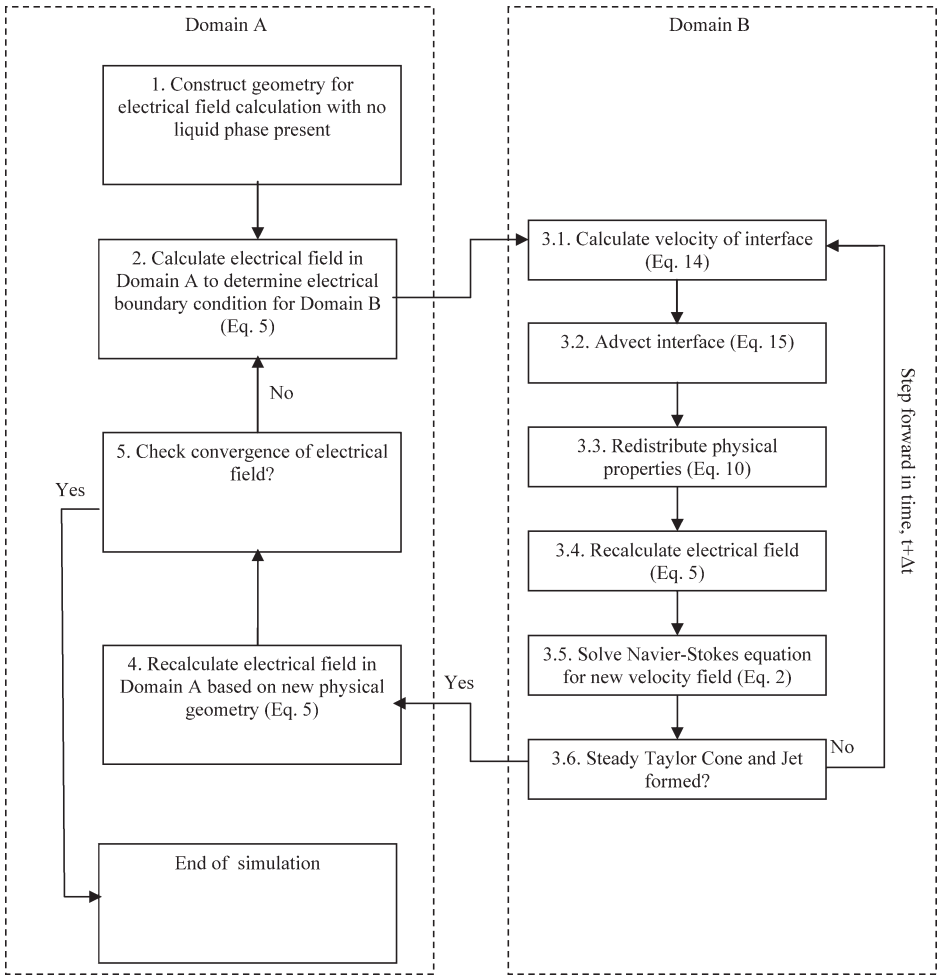

Figure 5. Flow chart for the iterative procedures in Domain A and Domain B, showing the linkage between the two computational procedures.

simulation, an outer loop for electrical potential field calculation in Domain A and an inner loop for CFD simulation of the liquid phase in Domain B (Figure 5). The procedures are listed below.

1. Individual EHDA elements (nozzle, ring electrode, and ground needle) are used for the initial calculation of the electrical field in the entire EHDA computational domain A. No liquid phase is present in the initial estimation of the electrical field.
2. The data from the electrical potential field calculation for the Domain A is extracted and then applied onto Domain B as the boundary conditions of the detailed electrical potential field.
3. CFD simulation is carried out in Domain B, and proceeds iteratively for each time step through the steps listed below.
   - 3.1. Using the velocity field (time step t) on the background mesh and the moving interface position (time step t), the moving velocity (time step t) of the interface is calculated through interpolation using Eq. 14.
   - 3.2. The interface is moved explicitly at its interfacial velocity to a new location (time step $t + 1$).
   - 3.3. With the new interface location, the physical properties (such as density, viscosity, and permittivity) are redistributed throughout the simulation domain B, with appropriate values used for the liquid phase and the gas phase. At this point, the interface electric charge density is also imposed on the control volume where the interface lies.
   - 3.4. Using a quasi-electrostatic approach, the electrical field strength (time step $t + 1$) throughout the simulation domain B are calculated. The electrical field strength is used to calculate the electrical stress.
   - 3.5. The mass conservation equation and the Navier–Stokes equations, with the inclusion of the electrical stresses and surface tension, are then solved to give the new velocity field and pressure field (time step $t + 1$).
   - 3.6. Presence of the steady Taylor cone and jet is checked. The criteria for a stable Taylor cone and jet are that the cone angle and the jet diameter have reached constant values with increasing times. If the criteria are not met, repeat steps 3.1–3.6 to continue with the calculation for the next time step.

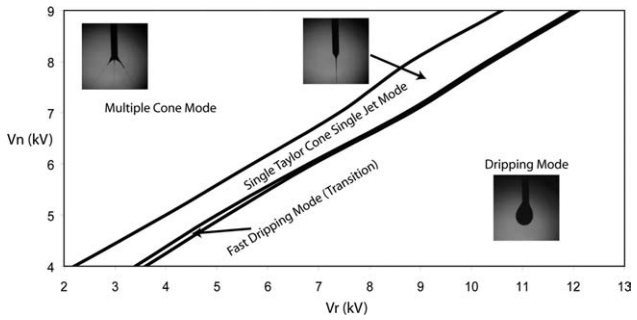

Figure 6. Map of different spray modes in an EHDA process when the nozzle electrical potential and the ring electrical potential are varied independently.

DCM flow rate = 6 ml/h. All other physical properties of DCM and air are based on the baseline parameter values mentioned in the text.

4. Once a constant Taylor cone and jet is reached, a new geometry for electrical potential field calculation on Domain A is created based on not only the nozzle, ring electrode, and ground needle but also the liquid phase (Taylor cone and jet) as determined from the previous CFD simulation in Domain B.
5. The electrical potential field calculation on Domain A is checked for convergence by comparing the electrical potential distribution on the location of Domain B boundaries in the initial estimation of the electrical potential field and the new estimation based on the presence of liquid phase. If convergence is not reached, another domain B with larger size is selected, and steps 2–5 are repeated. If convergence is reached, the selection of simulation B is finalized.

The simulations were performed on the IBM supercomputer p575 in the Institute of High Performance Computing, Singapore.

Results and Discussion

Electrical potential field

Experimental work was first performed to determine the stability map of the various spray modes when the nozzle and ring electrical potential were varied independently (Figure 6). As the nozzle electrical potential is increased, the spray mode changes from the gravity dripping mode to the single Taylor cone single jet mode, and finally to the multiple jet mode. Conversely, when the ring electrical potential is increased under high nozzle electrical potential, the spray mode changes from the multiple cone mode back to the single Taylor cone single jet mode, and finally to the gravity dripping mode. To investigate such findings, the electrical field near the nozzle is paid great attention in the present study, since the electrical field strength plays an important role on the EDHA process.

The electrical potential field is first calculated by solving the Poisson's equation in Domain A, which includes the nozzle, ring, and ground needle, using a software package FemLab (COMSOL®). Both the nozzle and ring electrodes are applied with constant electrical potential boundary conditions. A typical electrical potential is shown in Figure 7. From the contour of the electrical potential distribution, it can be observed that the electrical field is nonuniform over the whole domain, especially at the region near the nozzle tip, where the Taylor cone resides. It can be also noted that the contour lines of electrical potential nearby the cone-jet is significantly distorted by the low conductive liquid. This can be attributed to the difference in electric permittivity between the liquid phase and the gas phase, and the presence of electric charge at the interface as well.

Figure 8 shows the variations of electrical potential distribution on the right boundary of Domain B under the effects of the different settings of nozzle electrode (V_n) and ring electrode (V_r) electrical potentials. The electrical potential distribution on the right boundary of Domain B is the key input in determining the detailed electrical field distribution near the nozzle tip. Because of the linear characteristics of the electrical potential field, the electrical potential distribution on the right boundary of Domain B for any combinations of electrical potentials on the nozzle and the ring electrodes can be calculated by summing up the contributions from the nozzle electrical potential (Figure 8A) and the contribution of the ring electrical potential (Figure 8B). Thus, the magnitude of the electrical potential difference between the nozzle and the right boundary increases when the nozzle electrical potential is increased. In contrast, increasing the ring electrical potential with high electrical potential imposed on the nozzle has the opposite effect for decreasing the magnitude of the potential difference between the nozzle and the right boundary. The electrical potential difference has a direct relationship with the electrical field strength, as shown in Eq. 6. The electrical field strength thus increases with increasing V_n, but decreases with increasing V_r. As shown in Eq. 4, increasing the electrical field strength will increase the magnitude of the electrical stress. The electrical potential field thus constitutes an important boundary condition for the formation of the EHDA spray. Different combinations of nozzle and ring electrode potentials may produce similar electrical potential profiles on the boundary of the

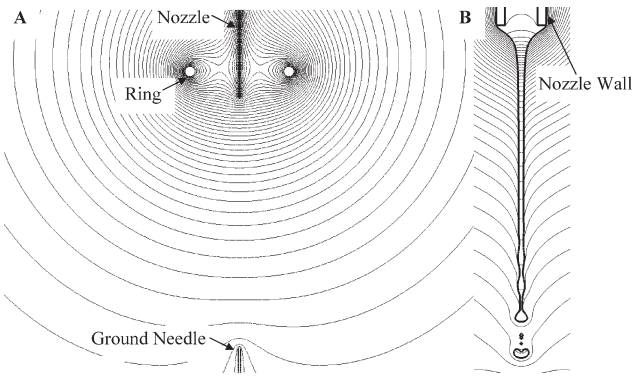

Figure 7. Electrical potential field when V_n is 8 kV, V_r is 7.9 kV.

A: Cross-sectional view, equipotential line of electrical potential field in Domain A. B: Cross-sectional view, equipotential line of electrical potential field in Domain B.

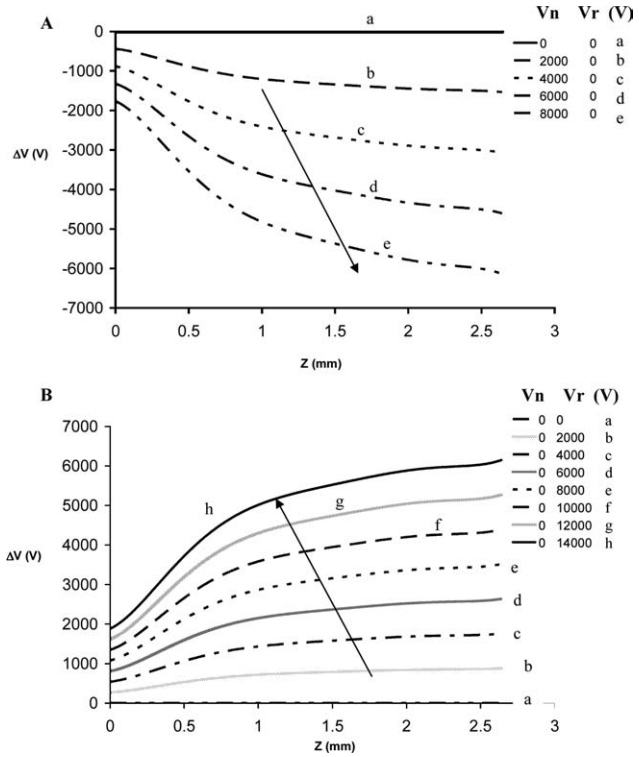

Figure 8. The changes in potential difference between the nozzle and the right wall (Figure 4) (ΔV).

The *x*-axis shows the *z* coordinates with the origin situated at the tip of the nozzle, pointing in the direction away from the nozzle. In contrast, the *y*-axis shows the potential differences between the nozzle and the right wall. A: Increasing the electrical potential on the nozzle increases the potential difference between the nozzle and the right wall. B: Increasing the electrical potential on the ring has the opposite effect.

system. For example, applying 5 kV on the nozzle and 0 kV on the ring will have the same electrical potential profile on the right boundary as the case applying 8 kV on the nozzle and 7 kV on the ring. Similar electrical potential profiles on the right boundary of the system will result in comparable effects on the cone-jet formation pattern. Increasing the nozzle electrical potential has the same effect on the electrical field strength near the nozzle tip as decreasing the ring electrical potential, resulting in similar spray mode. This exercise shows two important points. First, the far field effect needs to be taken into account for accurate depiction of the electrical field of the EHDA process. Second, the presence of the ring electrical potential could possibly serve as a means for the adjustment of the spray modes through controlling the electrical potential field near the spray nozzle. The advantage of such a controlling approach can be shown by in Figure 8. For a range of electrical field strength covered by increasing the nozzle electrical potential from 0 kV to 8 kV, the ring electrical potential would need to be changed from 0 kV to 14 kV. The map of spray modes of the EHDA system determined through experiments (Figure 6) also shows a similar trend, where for stable single Taylor cone single jet mode, the ring electrical potential has almost double the range as compared to the nozzle electrical potential. This shows that the nozzle electrical potential can serve as a coarse control of the EHDA spray, while the ring electrical potential would serve as a fine control of the EHDA spray.

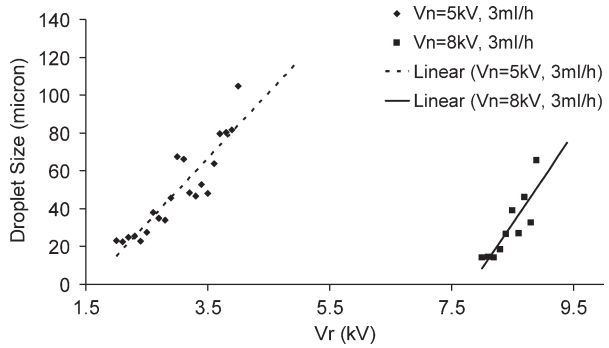

Figure 9. Experimental data (together with the corresponding linear fitting) on the changes in the droplet size when the ring electrical potential is varied.

The two data sets correspond to two different nozzle electrical potentials. The solution sprayed is pure dichloromethane. Droplet size was measured using a phase Doppler particle analyzer.

Droplet size also changes when the ring electrical potential is varied while maintaining the EHDA spray in the single Taylor cone single jet mode. In the experimental work performed, the droplets size of pure DCM was measured using a phase Doppler particle analyzer. The ring electrical potential is varied while the nozzle electrical potential is kept constant, first at 5 kV and later at 8 kV (Figure 9). As the ring electrical potential was increased, the droplet size was also increased. This simulation result highlights the possible engineering principle for fine-controlling the droplet size in an EHDA process.

Cone-jet formation

Through experiments using pure DCM as the liquid phase for the electrohydrodynamic atomization, the electrical

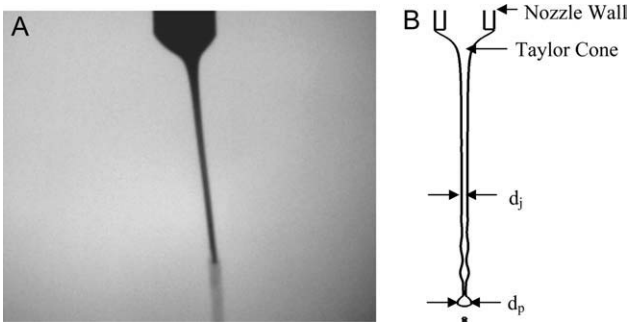

Figure 10. A: Backlit photo of the EHDA Taylor cone and jet. B: Simulated Taylor cone and jet. The solution used is dichloromethane. The nozzle electrical potential is 8 kV while the ring electrical potential is 8.9 kV.

It has a flow rate of 6 ml/h, and a surface charge density q^s of 2.688×10^{-5} C/m^2. d_j is the measured diameter of the jet, while d_p is the measured diameter of the droplets.

potential setting on the nozzle and the ring electrodes are determined and documented (e.g., Figure 10A). The electrical potential boundary conditions on the right boundary of Domain B are then calculated from the electrical field calculation in Domain A with the corresponding electrical potentials on the ring and nozzle electrodes. With the proper specification of electrical boundary conditions for Domain B, numerical simulations are then performed while varying of the value of interfacial electric charge so that a reasonably matched simulation results can be obtained.

A typical case of electrohydrodynamic atomization of HPLC grade dichloromethane was chosen for qualitative discussion purposes. In Figure 10, the electrical potential on the nozzle electrode is 8 kV, and the electrical potential on the ring electrode is 8.9 kV. The flow rate is 6 ml/h. Through the comparison between numerical simulations and experiments, the interfacial charge density is determined by fitting the simulated Taylor cone and jet profile with the experimental data (Figure 10).

Comparison of the experimental Taylor cone and jet profile in the single Taylor cone single jet mode with the simulation results in Figure 10 (Panel B) shows that the simulation is able to replicate the major qualitative feature of the Taylor cone and jet reasonably well. The Taylor cone is formed near the tip of the nozzle, and at this point, the liquid solution is accelerated due to application of electrical stresses so that radius of the liquid flow is reduced successively. From the tip of the Taylor cone, a jet is then formed that has a diameter of around one order of magnitude smaller than the diameter of the nozzle. This reduction in liquid jet diameter is the principal reason behind the ability of electrohydrodynamic atomization to form droplets that are smaller than the inner diameter of the nozzle. As the jet travels downward, interfacial instability sets in and droplets are then formed. Figure 11 shows the transient snap shots of the cone-jet formation process.

Figure 12 shows the changes in the spray mode when the electrical field strength is increased from left to right. To vary the electrical field strength, the ring electrical potential is varied. The simulation results agree well with the experimental results. At low electrical field strength, the electrical stresses are low such that the gravity-surface tension-dominant dripping mode can be observed. As the electrical field strength is increased by either changing the nozzle electrical potential or ring electrical potential, the single Taylor cone single jet mode is obtained, which is the mode where electrohydrodynamic atomization or electrospinning is usually performed. As the electrical field strength is increased further, multiple-cone-jet mode can be observed.

Inside the Taylor cone, the velocity field of the liquid is shown in Figure 13. The circulation of the liquid is found inside the Taylor cone. Only the liquid on the surface of the Taylor cone is accelerated towards the formation of the jet. This is due to the interaction between the electric charges at the liquid–gas interface and the electrical field, thus causing fluid motion on the interface along the tangential direction. Experimentally, such circulatory motion inside the Taylor cone has been reported by Shtern.[18] Similar results have been reported by Lastow[21] through numerical simulations. At the liquid jet, no circulation is present and the jet velocity field is unidirectional. Figure 14 shows the evolution of the velocity field when the Taylor cone is forming. During the formation period, the Taylor cone angle changes with time, and finally a stable Taylor cone with a jet from the tip could be obtained. The circulatory motion of fluid inside the Taylor cone will also form gradually when the Taylor cones progresses to a stable shape. In three-dimensional view, such circulatory motion would have a shape that is similar to a torus. In the initial period when the electrical stress is first exerted on the liquid–gas interface, a small circulation of fluid is first formed near the outer rim of the nozzle. The size of the circulation is small while the gap in the middle of the toroidal shaped circulatory motion is large. As the elapsed time increases, momentum transport occurs and the size of the circulation increases, until there is no gap in the middle of the toroidal shaped circulatory motion. The motion of fluid on the surface is in the direction away from the nozzle.

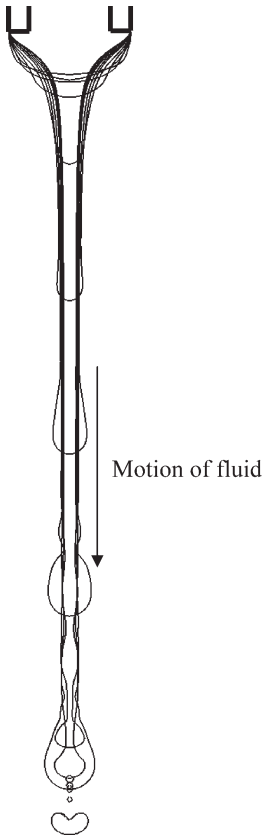

Figure 11. Snap shots of a typical cone-jet formation process.

The growth of the Taylor cone and jet is in the downward direction. The nozzle electrical potential is 8 kV while the ring electrical potential is 8.9 kV. It has a DCM flow rate of 6 ml/h, and a constant surface charge density q^s of 2.688×10^{-5} C/m^2 at the interface.

Droplet formation

At the end of the jet where droplets are formed, CFD simulation has shown the formation of the unstable wave like structure before the breakup of the jet (Figure 15). This is similar to the formation of droplets in surface tension driven

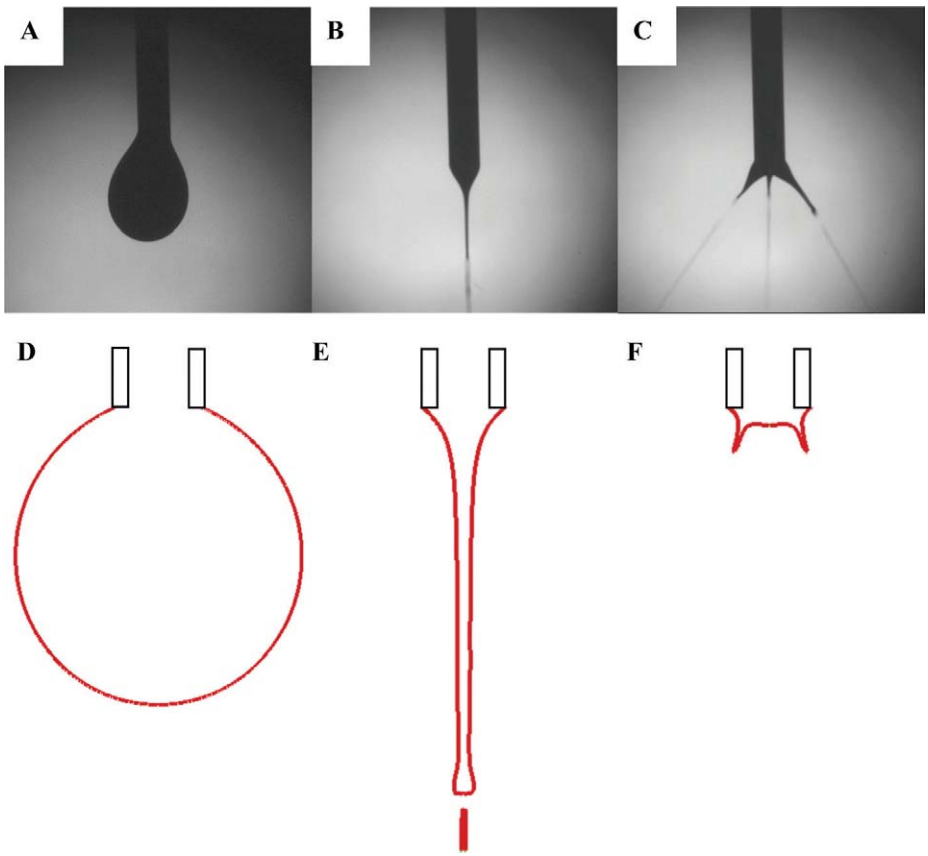

Figure 12. Comparison between experimental (A–C) and the corresponding simulated mode of DCM spray (D–F).

The electrical field strength near the nozzle is increased from left to right (A–C) by varying the electrical potential on the ring. The electric charge densities kept constant throughout. Panel D: (ϕ_n^*, ϕ_r^*, Re_E, Gr_E, Bo_E, El_P, El_C) = (1, 0.7753, 457.1, 433.4, 6.5, 17356.4, 29.5); Panel E: (ϕ_n^*, ϕ_r^*, Re_E, Gr_E, Bo_E, El_P, El_C) = (1, 1.1125, 457.1, 433.4, 6.5, 17356.4, 29.5); Panel F: (ϕ_n^*, ϕ_r^*, Re_E, Gr_E, Bo_E, El_P, El_C) = (1, 1.3371, 457.1, 433.4, 6.5, 17356.4, 29.5). [Color figure can be viewed in the online issue, which is available at wileyonlinelibrary.com.]

Rayleigh disintegration. Hohman[19] has reported the experimental observation of similar structure on the jet in EHDA. As the neck decreases in diameter due to surface tension, the jet will break into droplets of similar size as the jet diameter. The droplet size can be determined through direct measurements of the droplets simulated. In the EHDA process, assuming that the polymer-organic solvent mixture is a homogenous solution, the amount of polymer per droplet has a direct relationship to the droplet size. Hence, the droplet size can be varied by controlling the jet diameter in the EHDA process by adjusting the electrical potentials on the nozzle and ring electrodes and the charging density on the liquid–gas interface, which will finally affect the size of the particle fabricated.

In the EHDA process, the flow physics is dominated by two different scales. In the region nearby nozzle, viscous force is the dominating factor for Taylor cone formation, while the surface tension force dominates the jet formation and breakup into droplet. In the current numerical simulation, we consider both cone and jet.

The viscous flow time scale can be estimated by $\tau^V = \rho L^2/\mu$. The relevant physical properties of liquid dichloromethane are given by $\rho = 1360$ kg/m^3, $\mu = 4.3 \times 10^{-4}$ Pa s. The length scale of liquid flow can be estimated as the nozzle or drop diameter, about 100 μm. Hence, the time scale of the viscous flow is calculated as $\tau^V = 0.0316$ (s).

For the droplet formation process, the time scale of fluid flow is dominated by the surface tension, and the time scale can be estimated as $\tau^\gamma = \left(\rho L^3/\gamma\right)^{0.5}$. The surface tension coefficient is given by $\gamma = 0.025$ N/m, hence $\tau^\gamma = 2.33 \times 10^{-4}$ (s).

The charge relaxation time can be estimated by the following formula, $\tau^E = \varepsilon/K$. The relative permittivity is $\varepsilon = 8.73$, and the electric conductivity is about $K = 2.75 \times 10^{-8}$ S m. Hence, the time scale of charge relaxation is estimated as

$$\tau^E = (8.73 \times 8.85 \times 10^{-12}) \Big/ 2.75 \times 10^{-8} = 2.81 \times 10^{-3} (\text{s}).$$

By comparing the three time scales listed above, it can be concluded that the electrical relaxation time scale is smaller than the viscous/inertia one but larger than the surface tension/inertia one. Hence, the leaky dielectric model is not suitable for the system studied in this article (Leaky dielectric model may be suitable for simulating the formation of the Taylor cone, but not for the jet and droplet formation.)

The time interval used in Figure 15 is about 12 μs. The time step size used in the numerical simulation should be much smaller than the physical time scale so that the numerical simulation can capture the detailed physics. Twelve

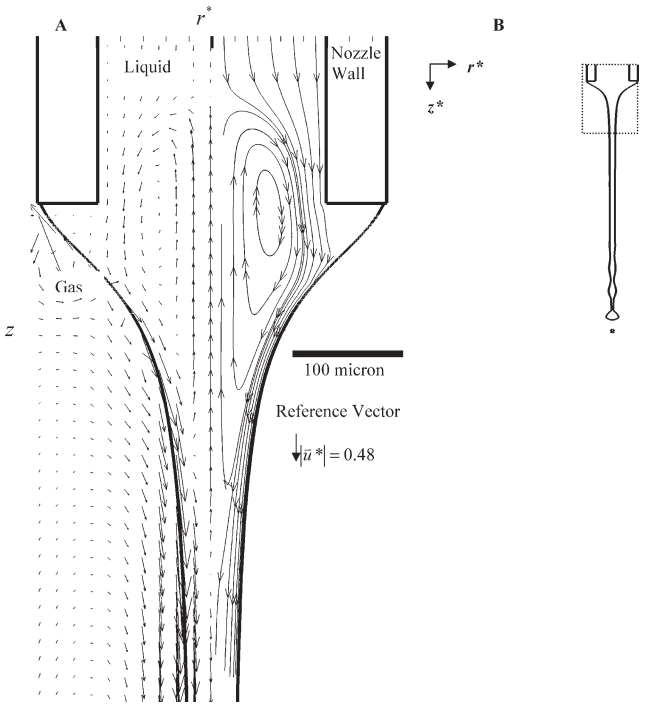

Figure 13. Dimensionless velocity field of the Taylor cone.

A: Velocity field represented by velocity vector is plotted on the left. Streamline of the liquid flow is plotted on the right. B: Location of the plotted region relative to flow (Figure 4). $\phi_n^* = 1$, $\phi_r^* = 1.1125$, $Re_E = 457.1$, $Gr_E = 433.4$, $Bo_E = 6.5$, $El_P = 17356.4$, $El_C = 29.5$.

microsecond are able to give good continuous snap shots on the Taylor cone generation process.

Effect of the ring electrical potential and interfacial charge density on the Taylor cone and jet formation

One of the most interesting points in the electrohydrodynamic atomization process is the formation of a stable Taylor cone and the jet diameter is closely related to the Taylor cone angle. In the experimental work, the Taylor cone angle varied when the ring electrical potential was changed. In our previous work,[7] it was also found that the ring electrical potential can be used to control the size of the particle formed. To study this effect, the ring electrical potential is varied in the CFD simulations. Different dimensionless charge densities on the surface of the liquid were used. To impose the changes of ring electrical potential in the simulation, the electrical potential field is first simulated using Domain A with different ring electrical potentials, and later imposed on the CFD domain for the jet simulation.

Figure 16 shows the changes of Taylor cone and jet diameter when the ring electrical potential (V_r) and the interfacial charge density (q^s) were varied independently. By changing the ring electrical potential, the electrical field strength near the nozzle is varied accordingly. As shown in Figure 8, increasing the ring electrical potential can result in the reduction of the electrical field strength near the nozzle. Henceforth, as the ring electrical potential is reduced (with increasing electric field strength), the Taylor cone angle is increased, while the jet diameter is decreased. On the other hand, when the interfacial charge density is increased, the Taylor cone angle is again increased, while the jet diameter is decreased. In brief, when either the electrical field strength or the electric charge density is increased, the electrical stresses exerted on the interface increases, causing an increase in the Taylor cone angle and a decrease in the final jet diameter and droplet size.

In the single Taylor cone single jet mode of EHDA spray, when the ring electrical potential is increased, the cone angle decreases accordingly as observed in experiments shown in Figure 17. Attempts have been made to replicate such observation using CFD simulations. From the CFD results, it is interesting to note that a fixed charge density on the surface of the liquid would not be able to give reasonable prediction of the changes in the Taylor cone angle obtained in experiments (Figure 17). In fact, the simulations under-predict the reduction in Taylor cone angle when the ring electrical potential is reduced. The simulation results would fit the experimental results better only when the charge density on the surface of the liquid is reduced as well when the ring electrical potential is reduced. This suggests that the ring electrode, although having no direct contact with the sprayed solution, has an effect on the liquid charging process. Unfortunately, the complex electric charging process and the charge mobility problem are not included in the current CFD simulation. Henceforth, to obtain reasonable agreement between the experimental data and the simulation work, there is a need to first determine a suitable interfacial charge density under different ring electrical potentials. This can be achieved through matching the Taylor cone angle of the simulations using different charge densities with the experimental results. Armed with the interfacial charge density determined through the Taylor cone angle matching, the effect of ring electrical potential on the jet diameter and the droplet size can be discussed in a more physically realistic manner. For example, by reading Figure 17, when dimensionless ring electrical potential (ϕ_r^*) is set to 0.9875 (or equivalently $V_r = 7.9$ kV), the dimensionless interfacial charge density should (q^{s*}) be around 0.1506 (or equivalently $q^s = 6.27 \times 10^{-5}$ C/m^2). While for the case where $\phi_r^* = 1.1125$ ($V_r = 8.9$ kV), the dimensionless interfacial charge density (q^{s*}) should be around 0.0861 (or equivalently $q^s = 3.58 \times 10^{-5}$ C/m^2).

As the ring electrical potential was varied, a change in the jet diameter was observed in the CFD simulations. As the ring electrical potential is increased, there is a slight increase in the jet diameter (Figure 18) when q is below 12. In simple terms, this can be explained by the fact that the electrical field strength is reduced as the ring electrical potential is increased. The imposed electrical stress on the surface of liquid is also lowered, and it causes the liquid flow to flow at a lower speed. Conservation of mass will thus dictate that the jet will increase in diameter to accommodate for the reduced liquid velocity. Using the interfacial charge density matching of Taylor cone angle, the dimensionless jet diameter for the case of $\phi_r^* = 0.9875$ was predicted to be about 0.16. In another case of $\phi_r^* = 0.1125$, the dimensionless jet diameter was predicted to be about 0.23.

A comparison of the droplet size obtained in the CFD simulations and experiments was performed when the ring

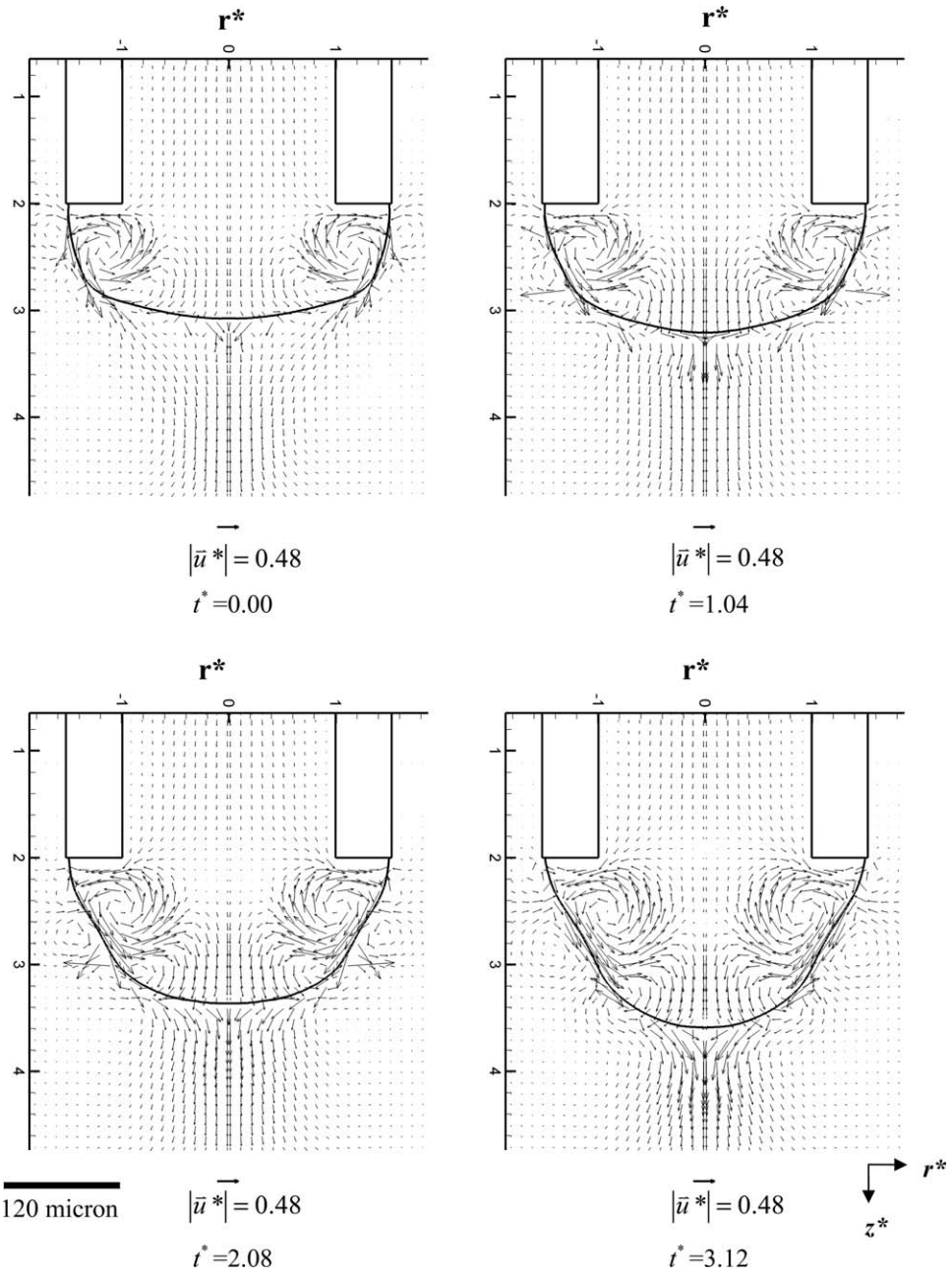

Figure 14. Velocity field evolution when the Taylor cone is initially formed.

The dimensionless time between snapshots $\Delta t = 0.104$. Reference scale for velocity vector is shown at the bottom of each plot. $\phi_n^* = 1$, $\phi_r^* = 1.1125$, $Re_E = 457.1$, $Gr_E = 433.4$, $Bo_E = 6.5$, $El_P = 17356.4$, $El_C = 29.5$.

electrical potential was varied. From the CFD simulations, it is found that the formed droplets size increases when the ring electrical potential is increased. The similar trend is observed in the experimental data (Figure 19). To get a more accurate prediction on the changes in droplet size, the charge density at the interface for the simulation of the Taylor cone, jet, and droplet formation should be first determined by matching the Taylor cone angle of the simulated results with the experimental results (Figure 17). As discussed, the most probable reason for the increase of droplet size with increasing ring electrical potential is that larger droplets can be obtained with the increase in jet diameter during the breakup stage.

As shown in Figure 6, there are several typical spray modes for the EHDA process (dripping drop, single cone-jet, and multiple cone-jets), depending upon the operation conditions. In our previous works,[5,6] the stable single cone-jet mode was the primary mode where fabrication of microparticles and nanoparticles was performed. Such previous experience dictates that it would be sensible to concentrate in looking into the stable single cone-jet mode with the current simulation method. Thus, to compare with experiments, our

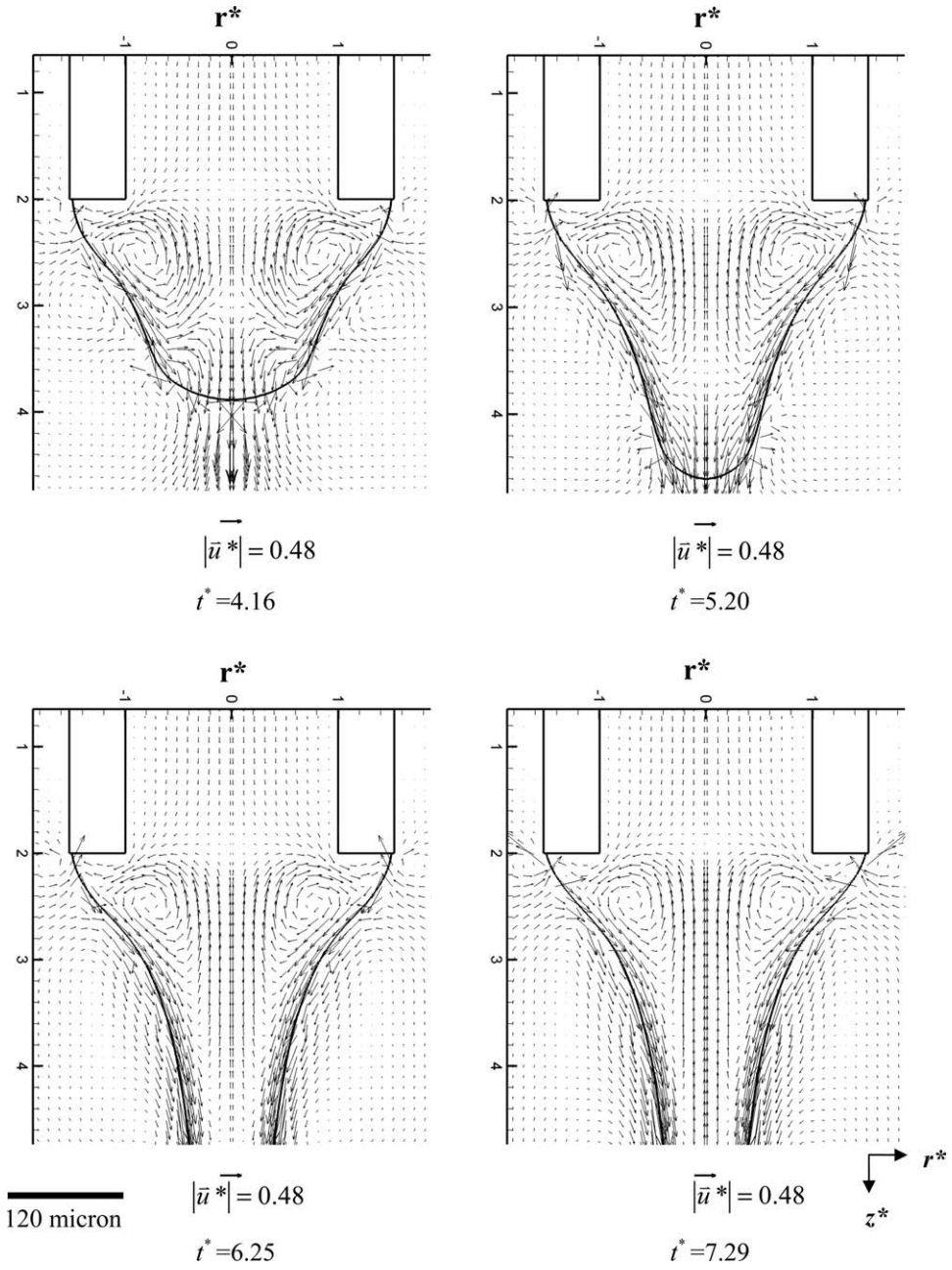

Figure 14. Continued.

simulations focus on the mode with single Taylor cone-jet. Our numerical simulations are based an axisymmetric model. In the experiments, we have observed the Taylor cone and jet with both DSLR still camera and high speed video camera to ensure that the Taylor cone and jet was stable. Only the DSLR still snap shot was presented due to the higher clarity of the picture. As pointed out by the reviewer, the snap shot photos of EHDA cone-jet shown in Figures 10 and 17 are not exactly axisymmetric. It is true that in experiments the axis of jet does not always align very well with the axis of nozzle due to some experimental uncertainties. In fact, the Taylor cone and jet produced with even a carefully aligned setup might still be affected by the surrounding environmental condition. The Taylor cone shape is characterized by the cone angle. It is defined as the side angle of a Taylor cone using the liquid jet as the axis. Normally, a series of photos of cone-jet were taken in an experiment. Averaged experimental values of cone angle are compared with those obtained in the simulations with the same operation conditions (includes the experimental setup, the electrical potential settings, the properties of the fluid phase used, etc.) in experiments. The effects of surface charge density are investigated by varying the surface charge density in the simulation. The surface charge density is determined when the simulation result fits experimental data well through the comparison of the Taylor cone angle

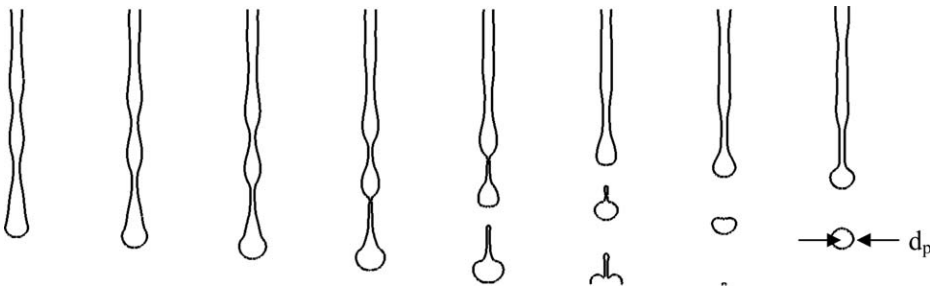

Figure 15. Unstable wave-like structure at the end of the liquid jet before pinch-off to form droplets.

Left to right: the evolution of droplets formation from jet. The interval between each frame is 12 ms. The liquid used is dichloromethane. The nozzle electrical potential is 8 kV while the ring electrical potential is 8.9 kV. It has a flow rate of 6 ml/h and constant surface charge density q^s of 2.688×10^{-5} C/m^2 at the interface. d_p Represents the measured diameter of the droplets.

of the simulated results and the Taylor cone angle measured using the still snap shots taken through experiments. Effect of surface charge density on the cone angle can be read from Figure 17.

Comparison between the constant surface charge model with the leaky dielectric model

No fully a priori model is available for fluids of low conductivity. We have therefore used a model for which the surface charge density is treated as a constant and is a fit parameter. The results are consistent with the experimental observations.

In the investigation of electrohydrodynamic atomization phenomena, many different methods in treating the surface charges have been proposed in the literature. In this study, the constant surface charge model has been used to simplify the treatment of surface charges as a preliminary step in developing the front tracking/finite difference numerical

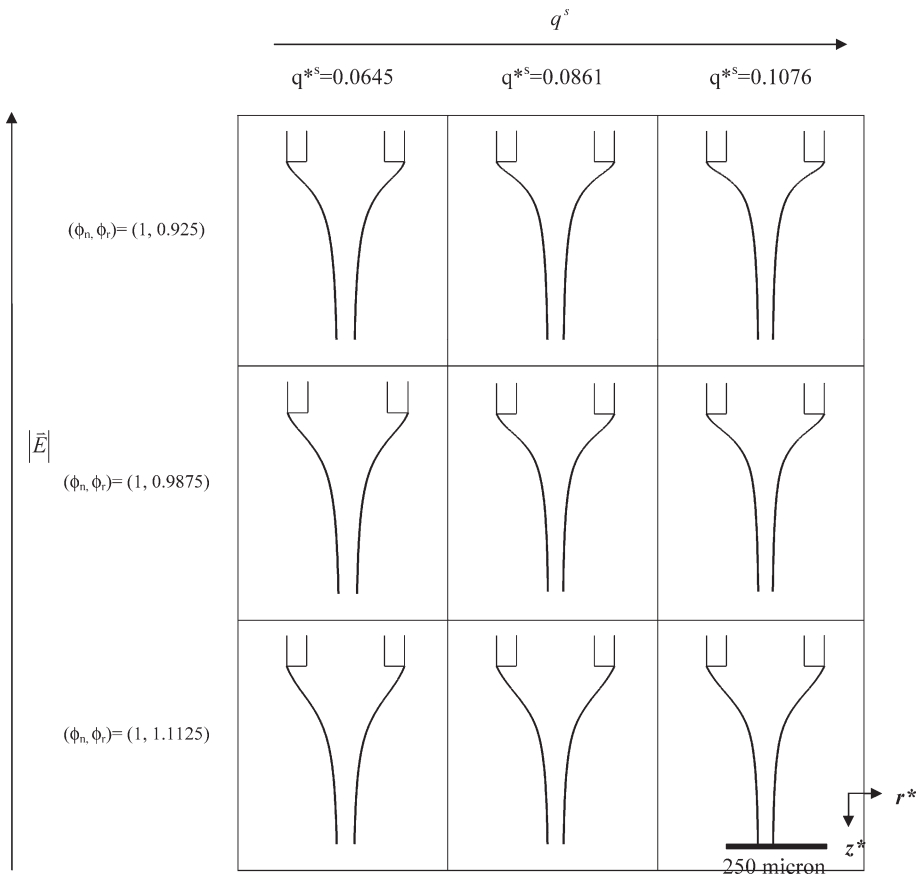

Figure 16. Changes in the Taylor cone when the surface charge density and the electrical field strength near the nozzle are varied independently.

The nozzle electrical potential is kept constant at $V_n = 8$ kV and a constant flow rate of 6 ml/h, while the dimensionless ring electrical potential ($\phi_r^* = \phi_r/\phi_n$) is varied. $Re_E = 457.1$, $Gr_E = 433.4$, $Bo_E = 6.5$, $El_P = 17356.4$, $El_C = 29.5$.

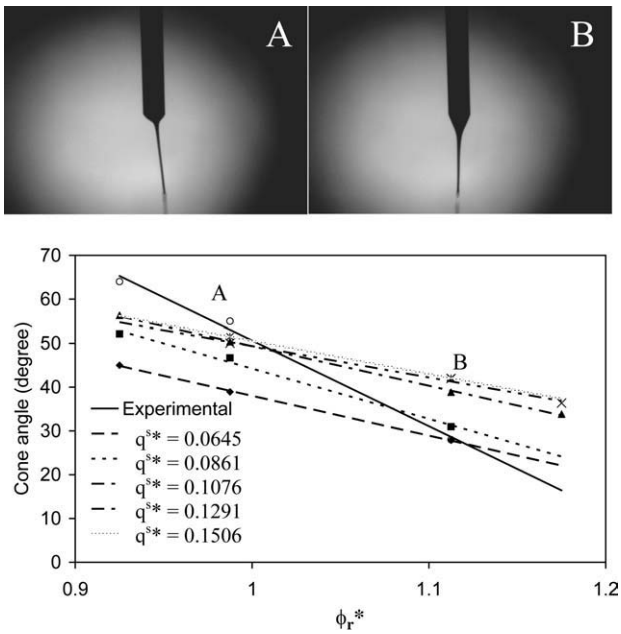

Figure 17. Changes in the cone angle when the ring electrical potential (ϕ_r*) is increased.

The nozzle electrical potential is kept constant at $\phi_n* = 1$. Similar trend is observed in the experimental data and in the simulated results. A and B represent the corresponding ring electrical potentials in both experimental and simulation results. The liquid used is dichloromethane. It has a flow rate of 6 ml/h, and different dimensionless charge densities, q^{s*}, were used on the surface of the liquid. $\phi_r* = 0.925$, 0.9875, 0.1.1125, and 1.175 correspond to $V_r =$ 7.4 kV, 7.9 kV, 8.9 kV, and 9.4 kV, respectively. The relevant dimensionless number for the different surface charge density can be found in Table 1. Top: Photographs of Taylor cone. Bottom: Comparison of experimental and simulation data.

methods. Hence, a holistic method in simulating both the Taylor cone and jet together can be developed.

In the leaky dielectric method, it was generally assumed that the electrical charge relaxation time scale is much smaller than the viscous timescale, so that electrical charge relaxes to the surface instantaneously, and a quasi-static state exist. To determine the electrical volume charge density around the liquid air interface, the Poisson's equation was used,

$$\rho^{f*} = \nabla \cdot \varepsilon^* \vec{E}^* \tag{29}$$

Table 1. Dimensionless Parameter Values Corresponding to Variations in the Surface Charge Density

	q^{s*} = 0.0645	q^{s*} = 0.0861	q^{s*} = 0.1076	q^{s*} = 0.1291	q^{s*} = 0.1506
Re_E	457.1	609.5	761.9	914.3	1066.6
Gr_E	433.4	770.6	1204.0	1733.7	2359.8
Bo_E	6.6	11.7	18.3	26.3	35.8
El_P	17356.4	30855.8	48212.2	69425.5	94495.9
El_C	29.5	52.5	82.0	118.0	160.6

$\phi_n^* = 1$.

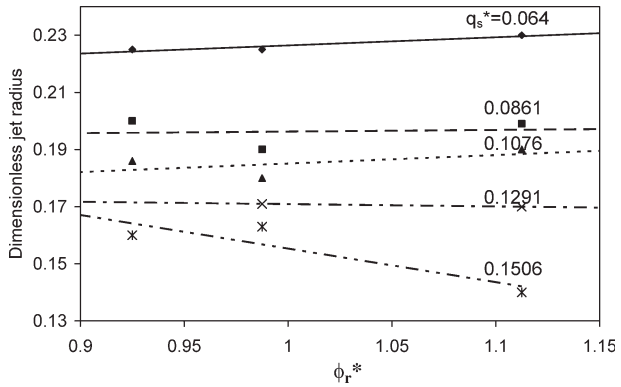

Figure 18. Changes in the jet diameter as the surface charge density and the ring electrical potential (ϕ_r*) are varied.

The nozzle electrical potential is kept constant at $\phi_n^* = 1$. Dimensionless ring voltage $\phi_r* = 0.925$, 0.9875, 0.1125 correspond to $V_r = 7.4$ kV, 7.9 kV, and 8.9 kV, respectively. The relevant dimensionless number for the different surface charge density can be found in Table 1. The liquid used is dichloromethane with a flow rate of 6 ml/h.

The electrical field is then a pre-requisite before the electrical volume charge density can be calculated. The assumption that the electrical charge relaxation time is small implies that the electrical charge conduction process dominates. In this case, the electrical field can be calculated using the electrical conductivity (K) of the system,

$$\nabla \cdot K^* \vec{E}^* = 0 \quad \text{or} \quad \nabla \cdot K^* \nabla \phi^* = 0 \tag{30}$$

where ϕ* is the electrical potential field and can be calculated.

The assumption of leaky dielectric model that the electrical charge relaxation time scale is much larger than the viscous timescale implies that the electrical conductivity of the

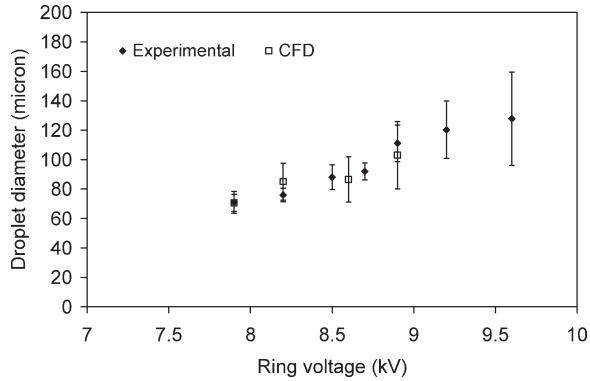

Figure 19. Changes in the droplet size when the ring electrical potential is changed.

The nozzle electrical potential is kept constant at 8 kV. Both simulation and PDPA experimental data are presented. The liquid used is dichloromethane, with a flow rate of 6 ml/h. A different charge density is imposed on the surface of the liquid, as determined empirically through the comparison of experimental and simulated Taylor cone angle data.

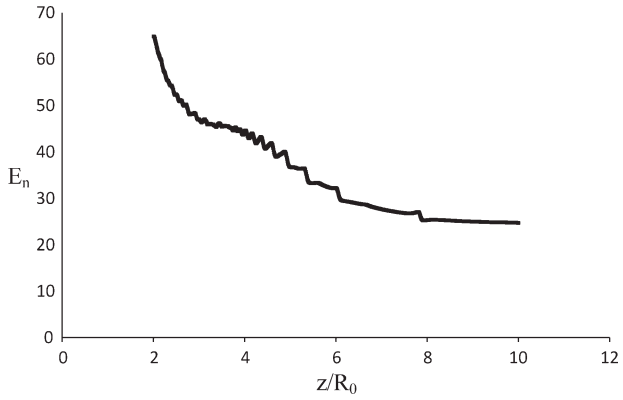

Figure 20. Variations on the normal component of electrical field (on the air side of the interface) with the traveling distance of the liquid away from the nozzle.

liquid under investigation is relatively high. In this study, the liquid used for investigating the EHDA phenomenon is HPLC grade dichloromethane, which instead has a low electrical conductivity. As discussed in a previous study by Hua et al.,[32] the constant surface charge model can be used instead as a step forward in modeling a low electrical conductivity fluid when it is charged. The presence of the electrical charges in the system will make the calculation of electrical field more directly by solving the following Poisson's equation,

$$\nabla \cdot \varepsilon^* \nabla \phi^* = \rho^{f*} \tag{31}$$

Also, as shown in Hua et al.,[32] the leaky dielectric model does not impart a net charge to the liquid system. To impart a net charge, the constant surface charge model was used instead in the present study. Although the constant surface charge model assumes a constant surface charge, it does not imply that the normal electrical field strength outside the interface is constant. As evident in Figure 20, the normal electrical field reduces in its strength as the interface travels further away from the nozzle. In fact, the normal electrical field is not constant since the electrical field has both components due to the electrical charge and the electrical field generated by the nozzle-ring-ground needle assembly.

Although the constant charge model and the leaky dielectric model treat the electrical charge in the system differently, a comparison of the simulations shows that the results by the two models are qualitatively similar as shown in Figure 21. On the left (Figure 21A) is the simulation results by Hothman and colleagues,[18] while on the right is the simulation results from the current work (Figure 21B). It can be seen that the qualitative feature of the change in jet radius (h), electrical potential on the air side of the interface (V), and the tangential electrical field on the interface (E) are similar in the Taylor cone jet when simulated using the two different models.

In actual situations, transport of electrical charges in a low conductivity fluid can be treated similarly as the transport of a molecular species. In this case, the motion of the electrical charge is determined by the full conservation of charge model. The equation for the conservation of electrical charge[27] can be derived through the electrical charge flux equation. However, since the equation needs to be coupled with the Navier–Stokes equation due to the presence of the convection term, it represents a great challenge to simulate such a system

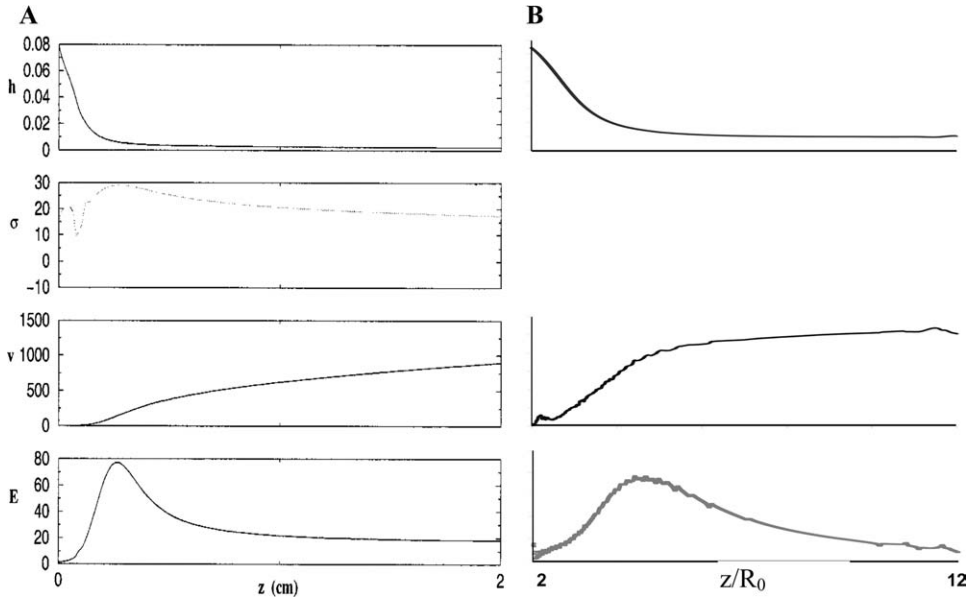

Figure 21. Comparison of simulated h, σ, v, and E values predicted by Hohman et al.[18] and the present study.

The graphs on the left (Panel A) are taken from the work by Hothman,[18] where the leaky dielectric model was used to treat the electrical charge in the EHDA system. The graphs on the right (Panel B) are from the present study, where the constant electrical surface charge model is used. It can be seen that the qualitative feature of the change in jet radius (h), electrical potential on the air side of the interface (V), and the tangential electrical field on the interface (E) are similar. [Panel A is Reproduced from Ref 18, with permission from American Institute of Physics].

numerically, but effort is currently underway by building on the basis of the constant charge model.

Conclusions

The addition of ring electrode, acting as a secondary electric field source in the electrohydrodynamic atomization process, has been found to be effective both in controlling the spray mode of the solution, and in fine controlling the size of the droplets formed. This method can be further extended to control the size of the particle formed in the range of micrometers and nanometers. A novel simulation approach was proposed in this article to make better prediction on the electrical potential distributions both in a large simulation domain including the effect of all electrodes and in a small simulation domain focusing on region near the nozzle tip. A front tracking/finite volume method has also been applied to simulate the electrohydrodynamic atomization process in the small simulation domain. By solving the Navier–Stoke equations with the addition of the electrical stresses and interface tension, the formation of Taylor cone, liquid jet, and the droplet in the EHDA process can be successfully replicated numerically. The current method has the advantage of being able to track the formation of the Taylor cone both temporally and spatially, and also has the ability to simulate the formation of the droplets from the jet breakup. As no decoupling of the Taylor cone and jet is required in the present model, a more realistic representation of the physics behind the EHDA process of a low conductivity liquid can be achieved. The comparison of the EHDA spray modes and the droplet size predicted by simulation with those observed from the experiments proves the reasonably good accuracy in the simulations. One limitation of the current simulation methodology is that the charging process on the liquid–gas interface is not predicted by a model, but is required as the simulation input. In addition, the distribution of charge on the liquid interface is assumed to be constant. Here, the interface charge density can be estimated by comparing the predicted Taylor cone angle with experimental observation. Nevertheless, the current numerical modeling method provides a platform for the in-depth investigation of effects of the surface charge density and the electrical potentials of the ring and nozzle electrodes on the EHDA process. As the fluid has a relatively low electric conductivity and the surface charge density is small, the current numerical simulation still makes reasonable predictions with the simplified electric charging model. Future studies may focus on the inclusion of the charging process into the simulation, and the detailed analysis of the jet breakup process of the charged jet under the influence of electrical field.

Acknowledgments

This research was supported by Agency of Science, Technology and Research (A*STAR) and National University of Singapore (NUS) under the grant number R279-000-208-305.

Notation

* = dimensionless variables
g = variables in the gas phase (air phase)
l = variables in the liquid phase (liquid solution phase)
$\vec{u}$ = velocity vector
ϕ = scalar electrical potential field relative to ground
E = vector electrical field
σ = surface tension at the liquid–gas interface
ε = electrical permittivity
P = pressure
κ = surface curvature
R_0 = radius of the nozzle
ρ = density
μ = dynamic viscosity
$\vec{g}$ = gravitational acceleration
q^s = interfacial (surface) charge density
q^v = space charge density

Literature Cited

1. Basset AB. Waves and jet in a viscous liquid. *Am J Math.* 1894;16:93–110.
2. Zeleny J. Instability of electrified liquid surfaces. *Phys Rev.* 1917;10:1–6.
3. Vonnegut B, Neubauer RL. Production of monodisperse liquid particles by electrical atomization. *J Colloid Sci.* 1952;7:616–622.
4. Magaver RH, Outhouse LE. Note on the break-up of a charged liquid jet. *J Fluid Mech.* 1962;13:151–157.
5. Ding L, Lee T, Wang CH. Fabrication of monodispersed taxol loaded particles using electrohydrodynamic atomization. *J Control Release.* 2005;102:395–413.
6. Xie JW, Marijnissen JCM, Wang CH. Microparticles developed by electrohydrodynamic atomization for the local delivery of anticancer drug to treat C6 glioma in vitro. *Biomaterials.* 2006;27:3321–3332.
7. Xie JW, Lim LK, Phua YY, Hua JS, Wang CH. Electrohydrodynamic atomization for biodegradable polymeric particle production. *J Colloid Interface Sci.* 2006;302:103–112.
8. Cloupeau M, Prunet-Foch B. Electrohydrodynamic spraying functioning modes: a critical review. *J Aerosol Sci.* 1994;25:1021–1036.
9. Jaworek A, Krupa A. Classification of the modes of EHD spraying. *J Aerosol Sci.* 1999;30:873–893.
10. Glonti GA. On the theory of the stability of liquid jets in an electrical field. *J Exp Theor Phys.* 1958;34:917–918.
11. Nayyar NK, Murty GS. The stability of a dielectric liquid in the presence of a longitudinal electrical field. *Proc Phys Soc London.* 1960;75:369–373.
12. Saville DA. Electrohydrodynamic stability: fluid cylinders in longitudinal electrical field. *Phys Fluid.* 1970;13:2987–2994.
13. Mestel AJ. Electrohydrodynamic stability of a slightly viscous jet. *J Fluid Mech.* 1994;274:93–113.
14. Hohman MM, Shin M, Rutledge G, Brenner MP. Electrospinning and electrically forced jets. I. Stability theory. *Phys Fluid.* 2001;12:2201–2220.
15. Melcher JR, Taylor GI. Electrohydrodynamics: a review of the role of interfacial shear stresses. *Annu Rev Fluid Mech.* 1969;1:111–146.
16. De la Mora JF. The fluid dynamics of Taylor cones. *Annu Rev Fluid Mech.* 2007;39:217–243.
17. Shtern V, Barrero A. Striking features of fluid flows in taylor cones related to electrosprays. *J Aerosol Sci.* 1994;25:1049–1063.
18. Hohman MM, Shin M, Rutledge G, Brenner MP. Electrospinning and electrically forced jets. II. Applications. *Phys Fluid.* 2001;12:2221–2236.
19. Hartman RPA, Brunner DJ, Camelot DMA, Marijnissen JCM, Scarlett B. Electrohydrodynamic atomization in the cone-jet mode physical modeling of the liquid cone and jet. *J Aerosol Sci.* 1999;30:823–849.
20. Yan F, Farouk B, Ko F. Numerical modeling of an electrostatically driven liquid meniscus in the cone-jet mode. *J Aerosol Sci.* 2003; 34:99–116.
21. Lastow O, Balachandran W. Numerical simulation of electrohydrodynamic (EHD) atomization. *J Electrostat.* 2006;64:850–859.
22. Unverdi SO, Tryggvason G. A front-tracking method for viscous, incompressible multi-fluid flow. *J Comput Phys.* 1992;100:25–37.
23. Hua JS, Lou J. Numerical simulation of bubble rising in viscous liquid. *J Comput Phys.* 2007;222:769–795.
24. Tryggvason G, Bunner B, Esmaeeli A, Juric D, Al-Rawahi N, Tauber W, Han J, Nas S, Jan YJ. A front tracking method for computations of multiphase flow. *J Comput Phys.* 2001;169:708–759.

25. Ijsebaert JC, Geerse KB, Marijnissen JCM, Lammers JWJ, Zanen P. Electrohydrodynamic atomization of drug solution for inhalation purposes. *J Appl Physiol*. 2001;91:2735–2741.
26. Saville DA. Electrohydrodynamics: the Taylor-Melcher leaky dielectric model. *Ann Rev Fluid Mech*. 1997;29:26–64.
27. Nelson JK. Dielectric fluids in motion. *IEEE Electr Insul Mag*. 1994;10:16–29.
28. Ganan-Galvo AM, Davila J, Barrero A. Current and droplet size in the electrospraying of liquids, scaling laws. *J Aerosol Sci*. 1997;28: 249–275.
29. Peskin CS. Numerical analysis of blood flow in the heart. *J Comput Phys*. 1977;25:220–252.
30. Peskin CS, Printz BF. Improved volume conservation in the computation of flows with immersed boundaries. *J Comput Phys*. 1993;105:33–46.
31. Patankar SV. *Numerical Heat Transfer and Fluid Flow*. Washington, DC: Hemisphere, 1980.
32. Hua JS, Lim LK, Wang CH. Numerical simulation of deformation/motion of a drop suspended in viscous liquids under influence of steady electric fields. *Phys Fluid*. 2008;20:113302.

Manuscript received Aug. 27, 2008, and revision received Mar. 6, 2010.